INTERNATIONAL JOURNAL FOR NUMERICAL METHODS IN FLUIDS
Int. J. Numer. Meth. Fluids (2008)
Published online in Wiley InterScience (www.interscience.wiley.com). DOI: 10.1002/fld.1797

On the use of anisotropic *a posteriori* error estimators for the adaptative solution of 3D inviscid compressible flows

Y. Bourgault[1,*,†], M. Picasso[2], F. Alauzet[3] and A. Loseille[3]

[1]*Department of Mathematics and Statistics, University of Ottawa, 585 King Edward Avenue, Ottawa, Ont., Canada K1N 6N5*
[2]*Institut d'Analyse et Calcul Scientifique, Ecole Polytechnique Fédérale de Lausanne, CH-1015 Lausanne, Switzerland*
[3]*INRIA, UR Rocquencourt, BP 105, F-78153 Le Chesnay Cedex, France*

SUMMARY

This paper describes the use of an *a posteriori* error estimator to control anisotropic mesh adaptation for computing inviscid compressible flows. The *a posteriori* error estimator and the coupling strategy with an anisotropic remesher are first introduced. The mesh adaptation is controlled by a single-parameter tolerance (TOL) in regions where the solution is regular, whereas a condition on the minimal element size $h_{\min}$ is enforced across solution discontinuities. This $h_{\min}$ condition is justified on the basis of an asymptotic analysis. The efficiency of the approach is tested with a supersonic flow over an aircraft. The evolution of a mesh adaptation/flow solution loop is shown, together with the influence of the parameters TOL and $h_{\min}$. We verify numerically that the effect of varying $h_{\min}$ is concordant with the conclusions of the asymptotic analysis, giving hints on the selection of $h_{\min}$ with respect to TOL. Finally, we check that the results obtained with the *a posteriori* error estimator are at least as accurate as those obtained with anisotropic *a priori* error estimators. All the results presented can be obtained using a standard desktop computer, showing the efficiency of these adaptative methods. Copyright © 2008 John Wiley & Sons, Ltd.

Received 1 November 2007; Revised 13 February 2008; Accepted 17 February 2008

KEY WORDS: compressible flows; anisotropic mesh adaptation; error estimators

1. INTRODUCTION

Anisotropic mesh adaptation has proved to be a powerful strategy to improve the quality and efficiency of compressible flow simulations, at first mostly for 2D flows [1–4]. These anisotropic

*Correspondence to: Y. Bourgault, Department of Mathematics and Statistics, University of Ottawa, 585 King Edward Avenue, Ottawa, Ont., Canada K1N 6N5.
†E-mail: ybourg@uottawa.ca

Contract/grant sponsor: Dassault Aviation

mesh adaptation techniques were initially based on a metric derived from a numerical approximation of the Hessian of the solutions with, in the background, the use of an *a priori* error estimator [5, 6]. The main idea behind the use of such metrics originates from the problem of finding the optimal mesh with a prescribed number of nodes, which minimizes the interpolation error of a given function [7, 8]. More recently, these *a priori* error estimators were used to drive unstructured mesh adaptation for 3D flows [9–11] and 3D phase change problems [12], just to name a few applications. For all these applications, sharp fronts, e.g. shocks in compressible flows or solidification interfaces, are meshed with high aspect ratio tetrahedra, allowing the computation of very accurate solutions with a minimal number of elements. These *a priori* error estimators successfully carry over to inviscid flows with shocks in spite of the fact that theoretically these estimates involve the Hessian of the exact solution, which is not regular. Practically, for these inviscid flows, flow solvers approximate regularized solutions (because of the artificial viscosity) with properly defined second derivatives that can be reconstructed with a recovery technique [13].

Following these works on metric-based anisotropic mesh adaptation, several anisotropic *a posteriori* error estimators were derived [14–20] and used to drive anisotropic mesh adaptation for a variety of problems in fluid dynamics, heat transfer and solidification [21–25]. These anisotropic *a posteriori* error estimators also turned out to be effective, although their complete mathematical justification and application were done only for problems involving second-order partial differential equations (PDEs). The extension of *a posteriori* error estimators to first-order PDEs is far from trivial. A limited number of attempts were done to obtain *a posteriori* estimators for first-order hyperbolic PDEs, for the pure advection equation [26], linear symmetric hyperbolic systems [27, 28], nonlinear scalar hyperbolic equations [29, 30], 1D nonlinear hyperbolic systems [31] and multi-dimensional nonlinear hyperbolic systems [32]. An estimator was proposed and tested for the linearized Euler equations for compressible flows [33]. A common feature of all these *a posteriori* error estimators for hyperbolic PDEs is that they are isotropic, in the sense that the orientation and shape of the elements are not accounted for in the estimators. Their modification into anisotropic estimators does not seem to be achievable. Moreover, aside from limited 2D test cases in [33], the practical efficiency at computing inviscid compressible flows of *a posteriori* error estimators, both in the isotropic and in the anisotropic cases, has not been looked at yet.

It is the purpose of this paper to look at the efficiency of an anisotropic *a posteriori* error estimator to compute 3D inviscid flows with shocks. We ought to show that in spite of its firm mathematical foundation for elliptic and parabolic equations only, anisotropic *a posteriori* error estimators can perform very well for inviscid flows when properly used. To reach our goal, we use the most recent anisotropic *a posteriori* error estimators of Picasso [20]. The goal of the project is to develop simulation capabilities for complex 3D external flows that run on simple workstations in a limited time and with limited memory.

This paper is organized as follows. Section 2 covers the numerical methods. The flow solver is based on a vertex-centered finite-volume method presented in [34]. We next present our *a posteriori* error estimator, and how it is coupled with the mesh adaptation software. An asymptotic analysis is then presented to assess the behavior of our *a posteriori* estimator when computing solutions with discontinuities. Section 3 presents numerical results. The test case is first detailed. All the simulations are based on the same external flow around a supersonic aircraft. The anisotropic adapted meshes are obtained within a solver/mesher loop using the `mmg3d` mesh adaptation software [35]. This software implements the local mesh modification techniques presented in [6]. After documenting this solver/mesher loop, the impact of the two main adaptation parameters associated with our *a posteriori* estimator is analyzed. We finish this section by briefly comparing

DOI: 10.1002/fld

our solutions with those obtained through the latest *a priori* error estimators developed in [13]. Section 4 presents the conclusions of our analysis.

2. NUMERICAL METHODS

2.1. Flow solver

We consider the set of Euler equations to model the flow. Assuming that the gas is perfect, nonviscous and that there is no thermal diffusion, the Euler equations for mass, momentum and energy conservation read

$$\frac{\partial \rho}{\partial t} + \nabla(\rho \mathbf{U}) = 0$$

$$\frac{\partial (\rho \mathbf{U})}{\partial t} + \nabla(\rho \mathbf{U} \otimes \mathbf{U}) + \nabla p = 0$$

$$\frac{\partial (\rho E)}{\partial t} + \nabla((\rho E + p)\mathbf{U}) = 0$$

where ρ denotes the density, $\mathbf{U}$ the velocity vector, $E = T + \|\mathbf{U}\|^2/2$ the total energy and $p = (\gamma - 1)\rho T$ the pressure with $\gamma = 1.4$ the ratio of specific heat and T the temperature. These equations could be symbolically rewritten as

$$\frac{\partial \mathbf{W}}{\partial t} + \nabla \cdot F(\mathbf{W}) = 0$$

where $\mathbf{W} = (\rho, \rho u, \rho v, \rho w, \rho E)^{\mathrm{T}}$ is the vector of conservative variables and the vector F represents the convective flux.

The Euler system is solved by means of a finite-volume technique on unstructured tetrahedral meshes [34, 36, 37]. The proposed scheme is vertex-centered and uses a particular edge-based formulation with upwind elements. This formulation consists in associating each vertex P_i of the mesh with a control volume or finite-volume cell C_i. The dual finite-volume cell mesh is built using the rule of medians. The common boundary $\partial C_{ij} = \partial C_i \cap \partial C_j$ between two neighboring cells C_i and C_j is decomposed into several triangular interface facets. We apply the finite-volume method to the Euler equations to obtain for each finite-volume cell C_i

$$|C_i| \frac{\mathrm{d}\mathbf{W}_i}{\mathrm{d}t} + \int_{\partial C_i} F(\mathbf{W}_i) \cdot \mathbf{n}_i \, \mathrm{d}\gamma = 0$$

where $\mathbf{W}_i$ is the mean value of the solution $\mathbf{W}$ on the cell C_i. The integral containing the convective flux F is computed by decomposing the cell boundary into its facets ∂C_{ij} and approximating the exact flux by a numerical flux function, denoted by Φ_{ij}

$$\int_{\partial C_i} F(\mathbf{W}_i^n) \cdot \mathbf{n}_i \, \mathrm{d}\gamma = \sum_{P_j \in \mathscr{V}(P_i)} F|_{I_{ij}} \cdot \int_{\partial C_{ij}} \mathbf{n}_i \, \mathrm{d}\gamma = \sum_{P_j \in \mathscr{V}(P_i)} \Phi_{ij}(\mathbf{W}_i, \mathbf{W}_j, \mathbf{n}_{ij})$$

where $\mathscr{V}(P_i)$ is the set of all neighboring vertices of P_i, $\mathbf{n}_i$ is the outer normal of the cell C_i, $\mathbf{n}_{ij} = \int_{\partial C_{ij}} \mathbf{n}_i \, \mathrm{d}\gamma$ and $F|_{I_{ij}}$ represents the constant value of $F(\mathbf{W})$ at the interface ∂C_{ij}. The

DOI: 10.1002/fld

numerical flux function approximates the convective terms on the common boundary ∂C_{ij}. This flow solver utilizes the HLLC approximate Riemann solver to compute the numerical flux [38].

A high-order scheme is derived according to the monotone upwind schemes for conservation laws (MUSCL) type method using downstream and upstream tetrahedra. This method provides a rather easy and, importantly, inexpensive higher-order extension of monotone upwind schemes. The idea is to use extrapolated values $\mathbf{W}_{ij}$ and $\mathbf{W}_{ji}$ of $\mathbf{W}$ at the interface ∂C_{ij} to evaluate the flux: $\Phi_{ij}=\Phi_{ij}(\mathbf{W}_{ij},\mathbf{W}_{ji},\mathbf{v}_{ij})$. To this end, we use a high-order gradient [39] $(\nabla\mathbf{W})_{ij}^{\mathrm{HO}}$ composed of centered gradient $(\nabla\mathbf{W})_{ij}^{\mathrm{C}}$ (i.e. the edge gradient) and upwind gradient $(\nabla\mathbf{W})_{ij}^{\mathrm{D}}$ (i.e. the upwind element gradient): $(\nabla\mathbf{W})_{ij}^{\mathrm{HO}}=\frac{2}{3}(\nabla\mathbf{W})_{ij}^{\mathrm{C}}+\frac{1}{3}(\nabla\mathbf{W})_{ij}^{\mathrm{D}}$. This numerical flux approximation is proved to be third order on a class of structured simplicial grids for linear advection.

Left as is, the scheme would not be monotone. The numerical flux needs to be limited to guarantee the total variation diminishing (TVD) property of the scheme. The considered limiter is a generalization of the Superbee limiter [36] with three entries

$$\mathrm{Lim}(\nabla^{\mathrm{C}},\nabla^{\mathrm{D}},\nabla^{\mathrm{HO}})=0 \qquad \text{if } \nabla^{\mathrm{C}}\nabla^{\mathrm{D}}\leqslant 0$$

$$\mathrm{Lim}(\nabla^{\mathrm{C}},\nabla^{\mathrm{D}},\nabla^{\mathrm{HO}})=\mathrm{Sign}(\nabla^{\mathrm{C}})\min(2|\nabla^{\mathrm{C}}|,2|\nabla^{\mathrm{D}}|,|\nabla^{\mathrm{HO}}|) \quad \text{else}$$

The time integration is an explicit time-stepping algorithm using a 5-stage, second-order strong-stability-preserving Runge–Kutta scheme that allows us to consider a Courant–Friedrichs–Lewy (CFL) coefficient of up to 4 [40].

With these features, the solver is then conservative, positivity-preserving and monotone (TVD) [36].

2.2. *A posteriori error estimator*

Let us now introduce our *a posteriori* anisotropic error estimator that has been derived for elliptic problems in [19, 20]. The goal is to obtain an error estimator for the $H^1(\Omega)$ semi-norm of the true error $e=u-u_h$, namely $\|\nabla e\|_{L^2(\Omega)}$. Here u and u_h denote a generic variable and its numerical approximate, respectively. This generic variable could be any of the variables appearing in the flow vector $\mathbf{W}$ or a composite variable obtained from these. We will opt for the second choice and use the local Mach number as variable u_h to calculate the error estimator. We will show that, even though the exact solution is not in $H^1(\Omega)$, this error estimator can be efficiently used to guide mesh adaptation and to obtain accurate numerical solutions. Our error estimator will be computable for any numerical solution u_h reading as a continuous $P1$ finite-element function on a given mesh $\mathscr{T}_h$, obtained with a finite-element method or a cell-vertex finite-volume method. This will be so, irrespective of whether or not the exact solution u contains discontinuities. Of course, some justification and adjustment in the adaptation strategy will be required when the exact solution loses its regularity. We will come back to that point in Section 2.4.

We use the notations of [14, 15] in order to describe the anisotropy of the mesh cells. The reader should note that similar results can be found in [16, 41]. For any tetrahedra K of the mesh $\mathscr{T}_h$, let $T_K:\hat{K}\to K$ be the affine transformation that maps the reference tetrahedra $\hat{K}$ into K. Let M_K be the Jacobian of T_K that is

$$\mathbf{x}=T_K(\hat{\mathbf{x}})=M_K\hat{\mathbf{x}}+\mathbf{t}_K$$

DOI: 10.1002/fld

As M_K is invertible, it admits a singular value decomposition $M_K = R_K^{\mathrm{T}} \Lambda_K P_K$, where R_K and P_K are orthogonal matrices and where Λ_K is diagonal with positive entries. In the following we set

$$\Lambda_K = \begin{pmatrix} \lambda_{1,K} & 0 & 0 \\ 0 & \lambda_{2,K} & 0 \\ 0 & 0 & \lambda_{3,K} \end{pmatrix} \quad \text{and} \quad R_K = \begin{pmatrix} \mathbf{r}_{1,K}^{\mathrm{T}} \\ \mathbf{r}_{2,K}^{\mathrm{T}} \\ \mathbf{r}_{3,K}^{\mathrm{T}} \end{pmatrix} \tag{1}$$

with the choice $\lambda_{1,K} \geqslant \lambda_{2,K} \geqslant \lambda_{3,K}$. Geometrically, assuming that the reference tetrahedra $\hat{K}$ can be inscribed in a unit sphere, the singular value $\lambda_{i,K}$ represents the length of the half-axis $r_{i,K}$ of the ellipsoid circumscribing the tetrahedra K.

The flow solution u_h satisfies the discrete systems $F_h(u_h) = 0$ obtained from an appropriate discretization of the Euler equations $F(u) = 0$.[‡] The residual $F(u_h)$ is obtained by substituting the numerical solution in the partial differential operator associated with the Euler equations. For all tetrahedra $K \in \mathcal{T}_h$, let $f_i, i = 1, 2, 3, 4$, be the four faces of the tetrahedra K, let $[\cdot]$ denote the jump of the bracketed quantity across f_i, with the convention $[\cdot] = 0$ for a face f_i on the boundary $\partial\Omega$. Then, our error indicator on tetrahedra K is defined by

$$\eta_K^2 = \left(\| F(u_h) \|_{L^2(K)} + \frac{1}{2} \sum_{i=1}^{4} \left(\frac{|f_i|}{\lambda_{1,K} \lambda_{2,K} \lambda_{3,K}} \right)^{1/2} \| [\nabla u_h \cdot \mathbf{n}] \|_{L^2(f_i)} \right) \omega_K(e) \tag{2}$$

Here $\mathbf{n}$ is the face unit normal (in arbitrary direction), e is again the true error and $\omega_K(e)$ is defined by

$$\omega_K^2(e) = \lambda_{1,K}^2 (\mathbf{r}_{1,K}^{\mathrm{T}} G_K(e) \mathbf{r}_{1,K}) + \lambda_{2,K}^2 (\mathbf{r}_{2,K}^{\mathrm{T}} G_K(e) \mathbf{r}_{2,K}) + \lambda_{3,K}^2 (\mathbf{r}_{3,K}^{\mathrm{T}} G_K(e) \mathbf{r}_{3,K}) \tag{3}$$

where $G_K(e)$ denotes the 3×3 matrix defined by

$$G_K(e) = \begin{pmatrix} \displaystyle\int_{\Delta_K} \left(\frac{\partial e}{\partial x_1} \right)^2 \mathrm{d}x & \displaystyle\int_{\Delta_K} \frac{\partial e}{\partial x_1} \frac{\partial e}{\partial x_2} \mathrm{d}x & \displaystyle\int_{\Delta_K} \frac{\partial e}{\partial x_1} \frac{\partial e}{\partial x_3} \mathrm{d}x \\ \displaystyle\int_{\Delta_K} \frac{\partial e}{\partial x_1} \frac{\partial e}{\partial x_2} \mathrm{d}x & \displaystyle\int_{\Delta_K} \left(\frac{\partial e}{\partial x_2} \right)^2 \mathrm{d}x & \displaystyle\int_{\Delta_K} \frac{\partial e}{\partial x_2} \frac{\partial e}{\partial x_3} \mathrm{d}x \\ \displaystyle\int_{\Delta_K} \frac{\partial e}{\partial x_1} \frac{\partial e}{\partial x_3} \mathrm{d}x & \displaystyle\int_{\Delta_K} \frac{\partial e}{\partial x_2} \frac{\partial e}{\partial x_3} \mathrm{d}x & \displaystyle\int_{\Delta_K} \left(\frac{\partial e}{\partial x_3} \right)^2 \mathrm{d}x \end{pmatrix} \tag{4}$$

The patch Δ_K is composed of the elements having at least one common vertex with the tetrahedra K.

Estimator (2) is not a usual error estimator since $e = u - u_h$ (and therefore u) is still involved. However, if we can guess e, then Equation (2) can be used to derive a computable quantity. This idea has been used in [19, 20] and an efficient anisotropic error indicator has also been obtained replacing the derivatives

$$\frac{\partial e}{\partial x_i} \quad \text{in (4) by} \quad \frac{\partial u_h}{\partial x_i} - \Pi_h \frac{\partial u_h}{\partial x_i}, \quad i = 1, 2, 3 \tag{5}$$

[‡]This F should not be confused with the flux F in the Euler equations.

DOI: 10.1002/fld

where Π_h is an approximate local $L^2(\Omega)$ projection onto the linear finite-element space V_h. More precisely, from constant values of $\partial u_h/\partial x_i$ on tetrahedron, we build values at vertices P of the mesh using the formula

$$\Pi_h\left(\frac{\partial u_h}{\partial x_i}\right)(P)=\frac{1}{\sum_{\substack{K\in\mathscr{T}_h\\P\in K}}|K|}\sum_{\substack{K\in\mathscr{T}_h\\P\in K}}|K|\left(\frac{\partial u_h}{\partial x_i}\right)_{|K},\quad i=1,2,3 \tag{6}$$

Approximating $\partial e/\partial x_i$ by $(I-\Pi_h)\partial u_h/\partial x_i$ is at the basis of the Zienkiewicz–Zhu error estimator [42, 43] and can be justified theoretically whenever superconvergence occurs, that is, when $\nabla u-\Pi_h\nabla u_h$ converges more rapidly to zero than $\nabla u-\nabla u_h$ in $L^2(\Omega)$. See [44–50] for theoretical results on the asymptotic exactness and convergence properties of the Zienkiewicz–Zhu error estimator. Numerical results show that the good properties of the Zienkiewicz–Zhu error estimator are underestimated by theoretical results, at least for elliptic and parabolic equations [19, 20].

The error estimator defined in Equation (2) approaches the true error on the numerical solution in the following sense:

$$C_1\sum_{K\in\mathscr{T}_h}\eta_K^2\leqslant\|\nabla e\|_{L^2(\Omega)}\leqslant C_2\sum_{K\in\mathscr{T}_h}\eta_K^2 \tag{7}$$

These estimators are proved for an elliptic equation [19, 20] as soon as the solution u is more regular than $H^1(\Omega)$, namely $u\in H^{1+\varepsilon}(\Omega)$ for any $\varepsilon>0$. The constant C_2 is always size and aspect ratio independent from the mesh, while the following equipartition condition is required for the constant C_1:

$$\lambda_{1,K}^2(\mathbf{r}_{1,K}^{\mathrm{T}}G_K(e)\mathbf{r}_{1,K})=\lambda_{2,K}^2(\mathbf{r}_{2,K}^{\mathrm{T}}G_K(e)\mathbf{r}_{2,K})=\lambda_{3,K}^2(\mathbf{r}_{3,K}^{\mathrm{T}}G_K(e)\mathbf{r}_{3,K}) \tag{8}$$

on all tetrahedra. This equipartition condition is the cornerstone behind our adaptation strategy, as will be detailed in Section 2.3.

From [41], it is known that face residuals dominate element residuals for finite-element methods applied to elliptic problems. This is fully justified for the Laplace equation, on both isotropic and anisotropic meshes. In [25] this has also been shown to work efficiently in practice for a 3D nonlinear partly parabolic problem describing the dendritic growth of a binary alloy. We assume that this is also valid for our problem and skip the residual term $\|F(u_h)\|_{L^2(K)}$ in the element error estimator η_K. This omission of the residual term makes the error η_K independent, at least formally, from the problem. This is a major gain as the computation of the element residual $F(u_h)$ is tedious for nonlinear problems such as the Euler equations for compressible flows. All our results presented below for the *a posteriori* error estimator have been obtained without the residual term. The element error estimator then reads as

$$\eta_K^2=\frac{1}{2}\sum_{i=1}^{4}\left(\frac{|f_i|}{\lambda_{1,K}\lambda_{2,K}\lambda_{3,K}}\right)^{1/2}\|[\nabla u_h\cdot\mathbf{n}]\|_{L^2(f_i)}\ \omega_K(e) \tag{9}$$

where $\omega_K(e)$ is defined by (3) and (4), and $G_K(e)$ is approximated from (5) and (6).

The Euler equations form a system of PDEs in five dependent variables. Although it is possible to extend the *a posteriori* estimator to systems by taking linear combinations of the estimator in each of the unknowns [21], we preferred to use a scalar 'compound' variable that varies in most of the flow regions (shock waves, rarefaction fans, etc.). A common choice is to use for u_h the local Mach number, i.e. the ratio of the local flow speed over the local speed of sound. This choice

DOI: 10.1002/fld

of compound variable has been shown to be particularly efficient at catching most flow features for inviscid, viscous and turbulent flows [3, 5, 34]. Other techniques are available for extending anisotropic error estimators to systems such as metric intersection [2] and dual problem methods [23]. These have not been pursued here.

2.3. Coupling of the error estimators with metric-based anisotropic mesh generators

We briefly recall the adaptive algorithm presented in [19, 20]. The goal is to build an anisotropic mesh such that the estimated relative error is close to a preset tolerance, TOL, namely

$$0.75\ \mathrm{TOL} \leqslant \frac{(\sum_{K\in\mathscr{T}_h}\eta_K^2)^{1/2}}{\|\nabla u_h\|_{L^2(\Omega)}} \leqslant 1.25\ \mathrm{TOL} \tag{10}$$

A sufficient condition to ensure the above inequalities is to equidistribute the error estimator by enforcing

$$\frac{0.75^2\ \mathrm{TOL}^2\|\nabla u_h\|^2_{L^2(\Omega)}}{N} \leqslant \eta_K^2 \leqslant \frac{1.25^2\ \mathrm{TOL}^2\|\nabla u_h\|^2_{L^2(\Omega)}}{N} \tag{11}$$

for all $K\in\mathscr{T}_h$, where N is the number of tetrahedra in the mesh $\mathscr{T}_h$. In practice, a mesh satisfying (11) is built

- by equidistributing η_K in the directions $\mathbf{r}_{1,K}$, $\mathbf{r}_{2,K}$ and $\mathbf{r}_{3,K}$ (controlling the directions of stretching of the tetrahedra) so that (8) is satisfied;
- by aligning the tetrahedra K with the eigenvectors of the error gradient $G_K(e)$.

All the adapted meshes presented in this paper are generated using the `mmg3d` software [6, 35]. Anisotropic mesh generators, such as `mmg3d`, usually expect a metric tensor $\mathscr{M}=\mathscr{M}(P)$ at each node P of a background mesh. Metric tensors $\mathscr{M}$ are positive-definite matrices with eigenvectors $\mathbf{q}_i$ and respective eigenvalues γ_i, $i=1,2,3$. More precisely

$$\mathscr{M}(P)=\begin{pmatrix}\mathbf{q}_1{}^{\mathrm{T}}\\ \mathbf{q}_2{}^{\mathrm{T}}\\ \mathbf{q}_3{}^{\mathrm{T}}\end{pmatrix}\begin{pmatrix}\gamma_1 & 0 & 0\\ 0 & \gamma_2 & 0\\ 0 & 0 & \gamma_3\end{pmatrix}(\mathbf{q}_1\ \ \mathbf{q}_2\ \ \mathbf{q}_3) \tag{12}$$

We should have the relation $\gamma_i=1/\lambda_i^2$ between the eigenvalue γ_i of the metric tensor $\mathscr{M}$ and the singular value λ_i of the matrix M_K appearing in the affine transformation T_K of Section 2.2, when both values are reported at the nodes of the mesh.

Simply said, anisotropic mesh generators aim at producing 'generalized anisotropic' Delaunay meshes with tetrahedra having edges of unit length in the metric [6]. In other words, the eigenvectors $\mathbf{q}_i$ control the orientation of the tetrahedron whereas $1/\sqrt{\gamma_i}$ represents the Euclidean width of the element along $\mathbf{q}_i$. To interface our *a posteriori* error estimator with any anisotropic mesh generator, we build a metric tensor at each node by setting $\mathbf{q}_i=\mathbf{r}_i$, with $\mathbf{r}_i$ the eigenvectors of the error gradient $G(e)$ this time computed at each node, and by specifying the γ_i to iteratively achieve (11)

DOI: 10.1002/fld

through the strategy explained above. See [19, Section 3.2] for algorithmic details on the passage from the element-based *a posteriori* error estimator to a metric tensor at the nodes.

2.4. Asymptotic analysis and minimal mesh size

The use of the *a posteriori* error estimator presented above cannot be theoretically justified for solutions that are not at least in the space $H^1(\Omega)$. Inviscid supersonic flows contain shock waves and contact discontinuities, resulting in solutions u that are only in $L^p(\Omega)$, $1 \leqslant p \leqslant \infty$, but not in $H^1(\Omega)$. Using the *a posteriori* error estimator (9), the goal of the mesh adaptation is to obtain

$$\left(\sum_{K \in \mathscr{T}_h} \eta_K^2 \right)^{1/2} \approx \mathrm{TOL} \quad \|\nabla u\|_{L^2(\Omega)} \tag{13}$$

resulting in an error in $O(\mathrm{TOL})$. By a simple asymptotic argument we wish to investigate the impact of the solution regularity on the ability to achieve (10).

Let us first consider the case of a regular solution. When $u \in H^2(\Omega)$, one easily derives an asymptotic behavior in $\sum_{K \in \mathscr{T}_h} \eta_K^2 \approx \|\nabla e\|^2_{L^2(\Omega)} = O(h^2)$ from inequalities (7). To emphasize the differences between regular and discontinuous solutions, let us evaluate the order of all the terms in relation (10). We suppose that all tetrahedra K of the adapted mesh $\mathscr{T}_h$ have a size $\lambda_{i,K} = O(h)$ along the three directions $\mathbf{r}_{i,K}$. There are thus $O(h^{-3})$ tetrahedra. From [48, Theorem 4.1] we obtain that $\tilde{G}_K = O(h^5)$, where $\tilde{G}_K$ denotes the matrix $G_K(e)$ with the error ∇e approximated by the Zienkiewicz–Zhu error estimator as in (5). Note that [48, Theorem 4.1] requires some more regularity on the solution, i.e. $u \in H^3(\Omega)$, and usual regularity assumptions on the mesh including a minimal angle condition. Using again that $\lambda_{i,K} = O(h)$, we deduce

$$\omega_K(e) = \left(\sum_{i=1}^{3} \lambda_{i,K}^2 (\mathbf{r}_{i,K}^{\mathrm{T}} G_K(e) \mathbf{r}_{i,K}) \right)^{1/2} = O(h^{7/2})$$

From a Taylor expansion the jump $[\nabla u_h \cdot \mathbf{n}]$ is in $O(h)$. We obtain

$$\frac{1}{2} \sum_{i=1}^{4} \left(\frac{|f_i|}{\lambda_{1,K} \lambda_{2,K} \lambda_{3,K}} \right)^{1/2} \|[\nabla u_h \cdot \mathbf{n}]\|_{L^2(f_i)} = O(h^{3/2})$$

hence $\eta_K^2 = O(h^5)$. The mesh $\mathscr{T}_h$ has $O(h^{-3})$ isotropic tetrahedra; therefore

$$\sum_{K \in \mathscr{T}_h} \eta_K^2 = O(h^2)$$

We recover the same asymptotic behavior as above. Now noticing that $\|\nabla u_h\|_{L^2(\Omega)} = \|\nabla u\|_{L^2(\Omega)} + O(h)$, we conclude that by imposing (10) while adapting the mesh in one way or another, we control the semi-norm error $\|\nabla e\|_{L^2(\Omega)}$ with the appropriate asymptotic rate when $\mathrm{TOL} \to 0$.

We now turn to the case of less regular solutions. For steady inviscid flows, solution discontinuities arise along fixed surfaces S_j in Ω, allowing the definition of components Ω_i on which the solution is regular. We assume that these 'regular' components and the surfaces of discontinuity cover the domain Ω in the sense that $\Omega = (\cup_i \Omega_i) \cup (\cup_j S_j)$. The error estimator η_K should behave on regular components Ω_i as in the case of regular solutions analyzed above. Solutions to hyperbolic systems typically remain bounded in $L^\infty(\Omega)$ with finite jumps on the surfaces S_i. At least

DOI: 10.1002/fld

this is what is observed in practice for many strictly hyperbolic systems and what is proven for scalar hyperbolic equations [51, 52]. If the numerical solution u_h happens to converge to the exact solution u (say in some space $L^p(\Omega)$), then ∇u_h is in $L^2(\Omega)$ for continuous $P1$ finite-element solutions u_h and any finite $h>0$, *but* ∇u_h *does not converge in* $L^2(\Omega)$ as $h \to 0$. Thus, there is no chance that the error ∇e can be controlled, *a fortiori* in $L^2(\Omega)$, in the vicinity of the surfaces S_j. To avoid the blow-up of the semi-norm $\|\nabla u_h\|_{L^2(\Omega)}$ in the adaptation criteria (10), we limit from below the singular values by imposing $\lambda_{i,K} \geqslant h_{\min}$, for all i, on all tetrahedra K where this condition is not met. In practice, this lower bound is restrictive only for $\lambda_{3,K}$ and in rare occasions for $\lambda_{2,K}$. The minimal mesh size $h_{\min}$ is chosen in such a way that on regular components Ω_i, TOL is large enough and $h_{\min}$ small enough for the condition on $\lambda_{i,K}$ not to be enforced.

To analyze the asymptotic behavior of the error estimator for solutions with finite jumps on a finite number of surfaces S_j, consider a continuous $P1$ finite-element function u_h taking different constant values on both sides of a plane S cutting the domain Ω. A natural hypothesis for the mesh $\mathcal{T}_h$ is that the plane S is contained in a narrow band one-tetrahedra thick with a size $h := h_{\min}$ in the direction normal to the plane. This narrow band can be meshed in any intermediate way between the following two extreme cases: (I) $O(h^{-2})$ isotropic tetrahedra with $\lambda_{i,K} = O(h)$, $i = 1, 2, 3$ and (II) $O(1)$ anisotropic tetrahedra with $\lambda_{i,K} = O(1)$, $i = 1, 2$, the directions $\mathbf{r}_{1,K}$ and $\mathbf{r}_{2,K}$ being tangent to the plane S, and $\lambda_{3,K} = O(h)$, the directions $\mathbf{r}_{3,K}$ being normal to the plane S. The two cases are illustrated in Figure 1. Studying these particular functions u_h is sufficient to estimate the leading order of the terms when applying the adaptation criteria (10) or (11).

We proceed with the analysis of Case I. The function u_h then has a gradient ∇u_h in $O(h^{-1})$ on the narrow band, zero elsewhere. It can be seen easily that $\partial u_h/\partial x_i - \Pi_h \partial u_h/\partial x_i = O(h^{-1})$ on elements K in the narrow band; hence, $G_K(e) = O(h)$ and $\omega_K(e) = O(h^{3/2})$. The jump $[\nabla u_h \cdot \mathbf{n}]$ being in $O(h^{-1})$ on the narrow band, we obtain

$$\frac{1}{2} \sum_{i=1}^{4} \left(\frac{|f_i|}{\lambda_{1,K} \lambda_{2,K} \lambda_{3,K}} \right)^{1/2} \|[\nabla u_h \cdot \mathbf{n}]\|_{L^2(f_i)} = O(h^{-1/2})$$

hence $\eta_K^2 = O(h)$ for the $O(h^{-2})$ tetrahedra in the narrow band and

$$\sum_{K \in \mathcal{T}_h} \eta_K^2 = O(h^{-1})$$

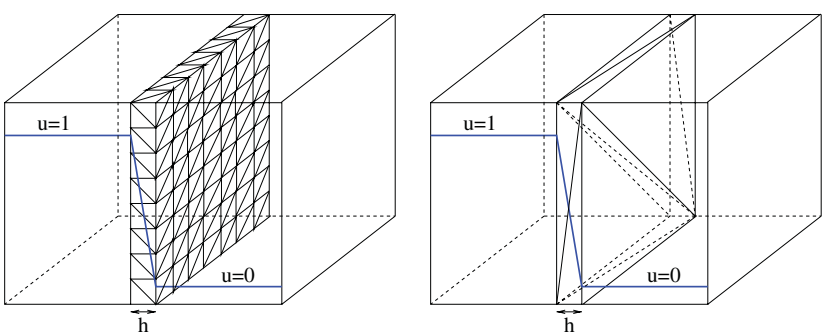

Case I: Isotropic mesh Case II: Anisotropic mesh

Figure 1. Illustration of the two extreme cases used in the asymptotic analysis.

DOI: 10.1002/fld

Similarly $\|\nabla u_h\|^2_{L^2(K)} = O(h)$ for $O(h^{-2})$ tetrahedra, which gives $\|\nabla u_h\|^2_{L^2(\Omega)} = O(h^{-1})$. For Case II there are $O(1)$ tetrahedra in the narrow band for which $\eta_K^2 = O(h^{-1})$, and we obtain the same asymptotic behavior in $O(h^{-1})$ for the global quantities $\sum_K \eta_K^2$ and $\|\nabla u_h\|^2_{L^2(\Omega)}$.

In both of these extreme cases, the ratio in the global adaptation criteria (10) is $O(1)$ and cannot be made arbitrary small by letting $\mathrm{TOL} \to 0$. We will see from our numerical results that this global ratio stabilizes after a number of mesher/solver iterations to a value relatively independent from $h_{\min}$ but which is not guaranteed to be within the 25% range around TOL as prescribed by (10). However, the situation is not as desperate with the local adaptation criteria (11). The local adaptation criteria (11) can properly be enforced away from the surface S_j, giving an appropriate error control of the form $\|\nabla e\|_{L^2(\Omega_i')} = O(\mathrm{TOL})$ for any open region Ω_i' strictly contained in a regular component Ω_i and not overlapping with the narrow bands of width $O(h_{\min})$ around the surfaces S_j. For the elements K within the narrow bands, Case I gives lower and upper bounds in $O(h\,\mathrm{TOL}^2)$ in (11) while $\eta_K^2 = O(h)$. For Case II the lower and upper bounds in (11) are in $O(\mathrm{TOL}^2/h)$ while $\eta_K^2 = O(1/h)$ around the surfaces S_j. It is impossible to let $\mathrm{TOL} \to 0$ to control the H^1 error over these elements. Instead the adaptation criteria (11) is switched off along $\mathbf{r}_{3,K}$ and the size of the tetrahedra is controlled by $h_{\min}$ in these regions. At best the numerical scheme used will guarantee that the L^p error on the numerical solution is a function of $h_{\min}$ around the S_j, at least for one $p \geqslant 1$. If $H^1(\Omega_i')$ can be injected continuously in $L^p(\Omega_i')$ for this same p, we control the global error in $L^p(\Omega)$ as a function of TOL and $h_{\min}$. The above argument is of course heuristic but this strategy based on the adaptation criteria (11) will turn out to be very efficient for computing inviscid flows with evidences showing that the mechanisms identified are the ones leading to very accurate results.

3. NUMERICAL RESULTS

Numerical results are presented for a 3D inviscid flow around a supersonic business jet provided by Dassault Aviation. We first introduce the test case and then present how the solver/mesher loop proceeds for a single set of the adaptation parameters TOL and $h_{\min}$. Next we look at the effect of varying these adaptation parameters on the quality of the solution, mesh characteristics, etc. Finally, we compare the results obtained with our *a posteriori* estimator with those obtained with the anisotropic *a priori* estimator introduced in [13]. In this section, we have replaced u_h by M_h to make explicit that the error estimators and the error on the solution are all computed using the local Mach number M_h instead of any of the flow variables ρ_h, $(\rho u)_h$, etc. The *a posteriori* error estimator η_K in (11) is computed from the local Mach number as if it is a continuous $P1$ finite-element variable.

3.1. Test case

The same test case is used for all the results presented. It is a steady inviscid flow over a generic supersonic business jet with a Mach number of 1.6 at infinity and an angle of attack of 3°. Figure 2 shows the initial mesh and a closeup of the aircraft, colored by the local Mach number of the flow. The Cartesian coordinate system has its origin located right on the back tip of the aircraft, the x-axis in the streamwise direction pointing downstream, the y-axis in the spanwise direction and the z-axis in the upward vertical direction. The business jet has a length of 37 units and is

DOI: 10.1002/fld

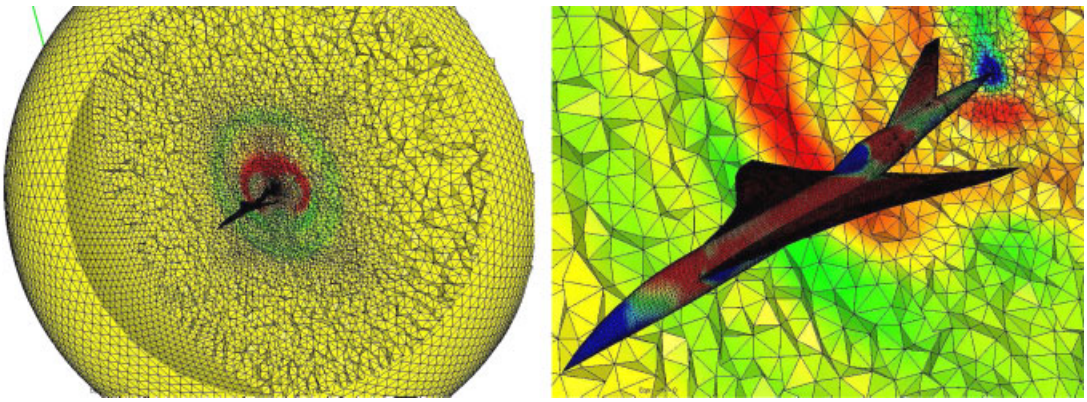

Figure 2. View of the initial mesh and initial solution (local Mach number).

included in a sphere of radius $R = 100$ with the center at the origin. A cut plane through the origin and perpendicular to the axis of the aircraft is included in the figure. The initial mesh is composed of 2 273 750 tetrahedra and 392 823 vertices. The tetrahedra are nearly isotropic, with small cells closer to the aircraft. The skin of the aircraft is meshed with triangles and is kept fixed during mesh adaptation. These triangles are taken small enough not to interfere with the quality of the solution, at least for the values of the mesh adaptation parameters used.

An initial solution is obtained on this initial mesh by starting from a uniform flow set to the condition at infinity and by doing about 500 time steps. A local time-stepping strategy is used to reach a steady solution in fewer time steps by enforcing a local CFL number of 0.8 on each cell, below the critical value 4.0 for the flow solver stability. The convergence of the solution toward a steady solution is checked by doing another 500 time steps and comparing the solutions 'with the eyes'. This is good enough to start our adaptation loop as we will do 500 time steps per adaptation/resolution cycle and about 50–100 cycles for a total of 25 000–50 000 time steps for reaching the final adapted solution.

Figure 3 shows one of the best solutions obtained with our mesh adaptation strategy. Details on the numerical parameters used to compute this solution will be given in Section 3.3. For now, we only mention that this solution has been obtained on a mesh with 6 928 342 tetrahedra and 1 193 575 vertices *on a simple desktop computer with 2 GB RAM in about 4.5 days of CPU time.* Unless otherwise stated, all the graphs showing the local Mach number presented in this paper are based on a truncated scale, meaning that areas with a local Mach number above 1.64 are colored in red whereas areas with a local Mach number below 1.54 are colored in blue. This has been done to amplify contrasts and better show the various details of the flow on the figures. The local Mach number usually stands between 1.1 and 2.1 with slight variations on the minimum and maximum from simulation to simulation.

Several shock waves and rarefaction fans can be seen in the figure. One of the strongest shocks is generated by the tip of the aircraft and can be seen as the leftmost passage from green to blue in the figures. This shock is attached to the tip and has a perfect conical shape. This shock wave is followed by a rarefaction fan induced by the curvature of the 'cockpit' (seen as a passage from blue to green and then yellow in the figures), and where the flow accelerates. Behind this rarefaction fan a weaker shock wave is generated at the wing/body junction (seen as passage from yellow to green in the figures). These rarefaction fan and weaker shock are difficult to compute numerically

DOI: 10.1002/fld

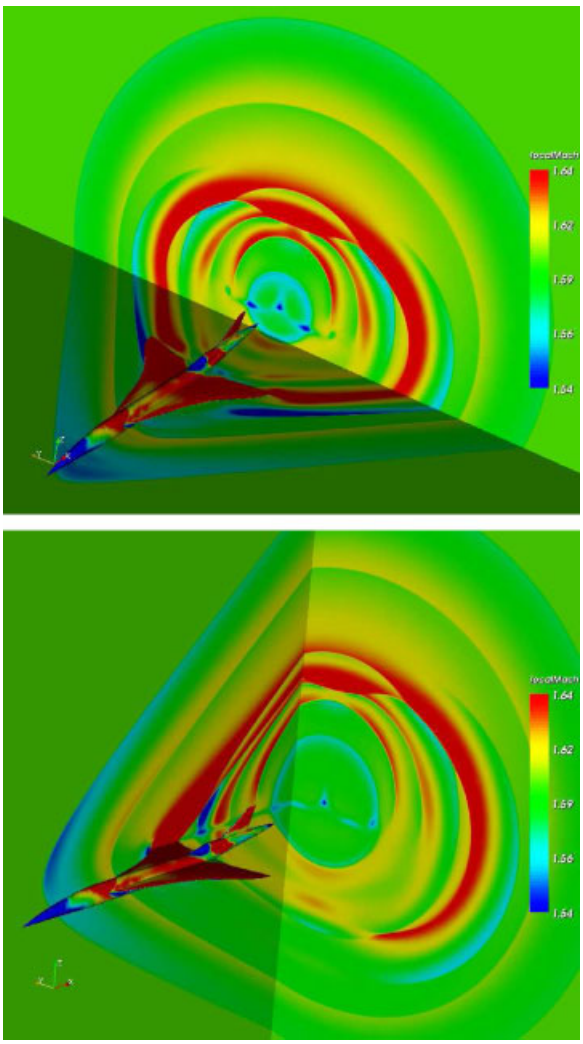

Figure 3. View of the adapted solution (local Mach number) on x- and z-normal planes (top figure), x- and y-normal planes (bottom figure).

and can be easily missed even with an adaptation procedure. Other shock waves are generated at the leading edges of the wing tips and empennage, at the bump preceding the empennage and as usual by the converging flows at the trailing edges of the wings, the empennage and the fuselage. The waves easily propagate far from the aircraft and interact together, leading to a complex flow with conflicting requirements in terms of anisotropic mesh adaptation.

3.2. Mesh adaptation/flow solution loop

We first present the evolution of the mesh and solution during the mesh adaptation/flow solution loop for the strategy sketched in Section 2.3. The results presented in this section have been obtained

DOI: 10.1002/fld

for TOL $=1.0$ and $h_{\min}=0.1$, doing 500 time steps with the flow solver between successive mesh adaptations.

Figures 4 and 5 show a cut of the meshes and solutions after 1, 5, 10 and 20 iterations of the mesher/solver loop. The cut is taken on the plane $x=0$, which is the vertical plane perpendicular to the symmetry plane of the aircraft and passing through the back tip (the origin) of the airplane. Clearly, the mesh is progressively refined and stretched close to the shock waves and coarsens away from these. Strong shocks are rapidly caught by the adaptive method, while weaker shocks take more mesher/solver iterations. The relatively strong conical shock created at the tip of the aircraft is focused between iterations 5 and 20. The weaker shock generated by the wing/body junction is not yet seen after 20 iterations. It is progressively refined between iterations 20 and 60, with the adapted region growing upward from the shock area below the aircraft. This weak wing/body junction shock can be seen on the final adapted mesh in Figure 9 (middle) after 100 mesher/solver iterations.

Table I shows the evolution of the mesh statistics with respect to the mesher/solver iterations. We can see a global decrease in the number of vertices and tetrahedra during the first 5 iterations followed by a progressive increase in these numbers toward a plateau corresponding to a converged adapted mesh (converged in a statistical sense). This results from the fact that the initial mesh is composed of a large number of isotropic cells. This mesh is fine enough to catch the gross features of the inviscid flow as can be seen in Figure 2, at least enough features to guide the

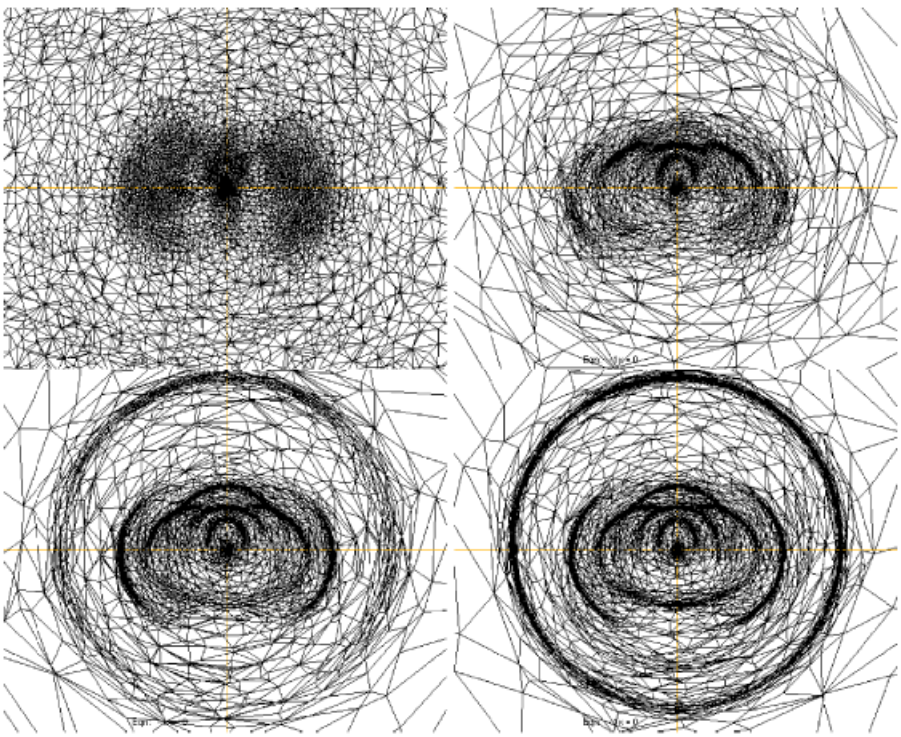

Figure 4. Meshes after 1 (top left), 5 (top right), 10 (bottom left) and 20 (bottom right) iterations of the meshing/solution loop.

DOI: 10.1002/fld

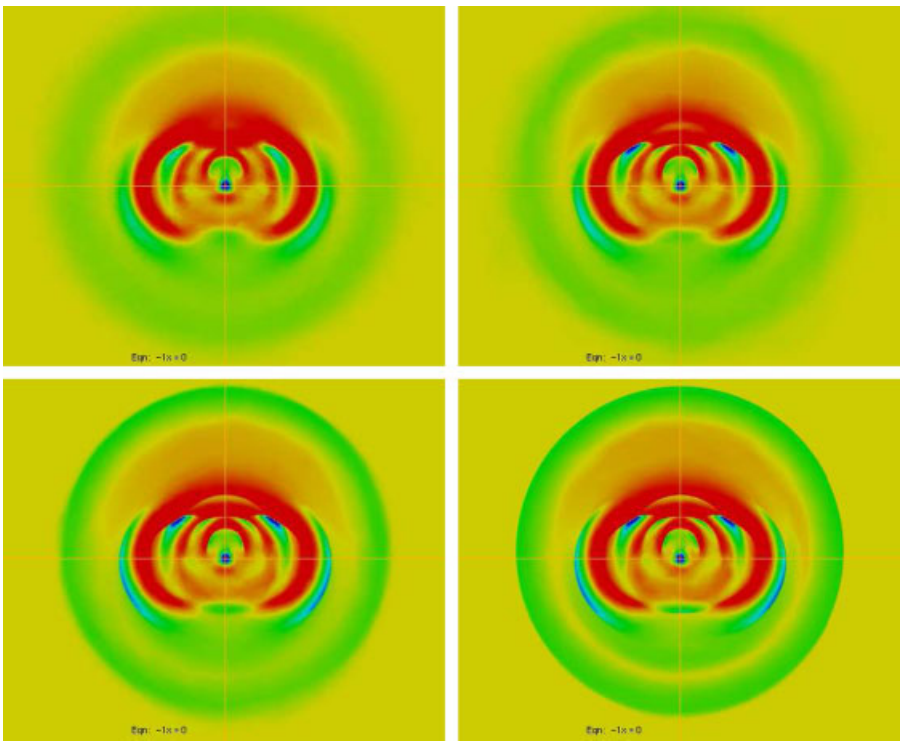

Figure 5. Solutions after 1 (top left), 5 (top right), 10 (bottom left) and 20 (bottom right) iterations of the meshing/solution loop.

Table I. Mesh statistics as a function of the mesher/solver iteration for TOL = 1.0 and $h_{\min} = 0.1$.

Iteration	0	1	5	10	20	50	100
No. nodes	392 823	221 306	107 045	122 396	156 450	183 158	194 533
No. tetrahedra	2 273 750	1 230 186	533 649	622 624	820 808	975 627	1 041 496
Average $\lambda_{1,K}$	2.56	2.35	2.32	2.61	3.30	4.09	4.62
Average $\lambda_{3,K}$	0.938	0.746	0.513	0.382	0.267	0.211	0.191
Average $\frac{\lambda_{1,K}}{\lambda_{3,K}}$	2.9	3.6	5.7	9.9	22.7	40.1	51.9
$\max_K \frac{\lambda_{1,K}}{\lambda_{3,K}}$	182.9	175.8	174.6	176.6	395.9	1507.1	1506.5
$\min_K \mathrm{vol}(K)$	4.91e−8	5.57e−8	6.48e−8	8.85e−8	8.96e−8	4.99e−8	4.12e−8
$\max_K \mathrm{vol}(K)$	8.37e1	5.33e2	2.42e4	5.98e4	5.56e4	5.45e4	7.76e4

early adaptation process. The initial mesh being uniformly fine, some of the regions (such as those of constant flow) are immediately required to coarsen. Other regions are refined and eventually stretched but this usually takes more solver/mesher iterations, hence this initial decrease is followed by an increase in the number of nodes and cells. The passage from an initial isotropic mesh to an adapted anisotropic mesh can be seen by looking at the average $\lambda_{1,K}$ that goes up with the iterations whereas the average $\lambda_{3,K}$ goes down. We recall that $\lambda_{1,K}$ corresponds to the size of the

DOI: 10.1002/fld

tetrahedra K along its direction $\mathbf{r}_{1,K}$ of maximal thickness and $\lambda_{3,K}$ to the size along its direction $\mathbf{r}_{3,K}$ of minimal thickness. The singular values $\lambda_{3,K}$ being divided by 5 on the average from the initial to the final adapted meshes, we may expect that an equivalent gain in accuracy using only isotropic splitting of the cells would be achieved by dividing the cell size by 5 in all three directions. The resulting isotropic mesh would then contain $5^3=125$ times as many cells or nodes as the initial mesh for the same accuracy as with our final anisotropic mesh. Note that our final anisotropic mesh contains less nodes than in the initial mesh. On the average, the tetrahedra K are 17 times more elongated in the final adapted mesh than the initial mesh. In comparison, the maximal elongation $\max_K \lambda_{1,K}/\lambda_{3,K}$ grows only by a factor of 8. A final average ratio $\lambda_{1,K}/\lambda_{3,K}$ of 51.9 indicates that the number of cells has to be multiplied by nearly $50^2=2500$ to transform the final adapted anisotropic mesh into an isotropic mesh guaranteeing the same accuracy on the solution. The minimal volume over all the cells K does not vary much during adaptation. For cells of minimal volume the decrease of $\lambda_{3,K}$ is most likely compensated by an increase in $\lambda_{1,K}$. The maximal volume grows by 3 orders of magnitude from the initial to the final meshes. This maximal volume corresponds to large cells that appear in the regions where the flow is constant but that were not present in the initial mesh.

Figure 6 shows the evolution of the ratio $(\sum_{K\in\mathcal{T}_h}\eta_K^2)^{1/2}/\|\nabla M_h\|_{L^2(\Omega)}$ that appears in the global adaptation criteria (10) for TOL$=$0.5, 1.0 and 2.0. For now we only comment on the curve for TOL$=$1.0. The other curves will be commented on Section 3.3. This ratio stabilizes in less than 20 mesher/solver iterations. The asymptotic ratio is 0.99, a value well within the 25% limit required by the global criteria (10). The local criteria (11) is thus efficient at controlling the global ratio in spite of a relatively large number of tetrahedra where the $h_{\min}$ condition spoils the adaptation process. Figure 7 gives a glimpse on these tetrahedra where $\lambda_{3,K}$ has been replaced by $h_{\min}$ (colored in red), at least for those tetrahedra in the vicinity of the plane $x=0$ normal to the axis of the aircraft. Clearly, the $h_{\min}$ condition applies in the shocks where the flow variables jump.

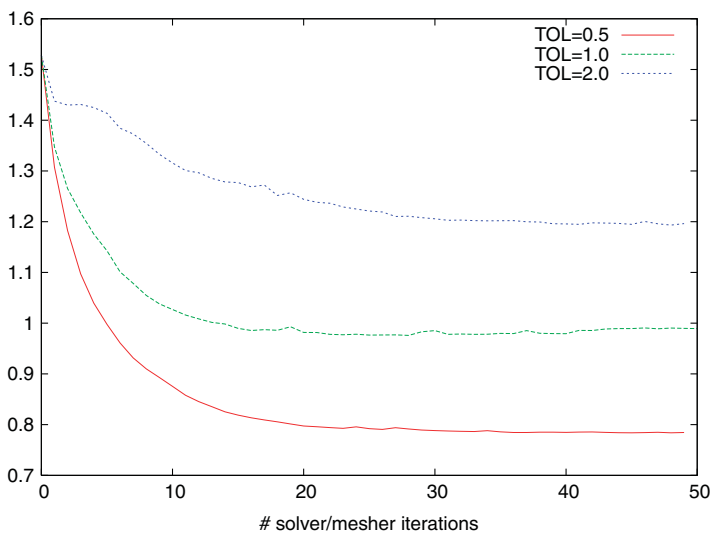

Figure 6. Ratio of the error estimator over $\|\nabla M_h\|_{L^2(\Omega)}$ (see Equation (10)) as a function of the mesher/solver iterations for $h_{\min}=0.1$ and various TOL.

DOI: 10.1002/fld

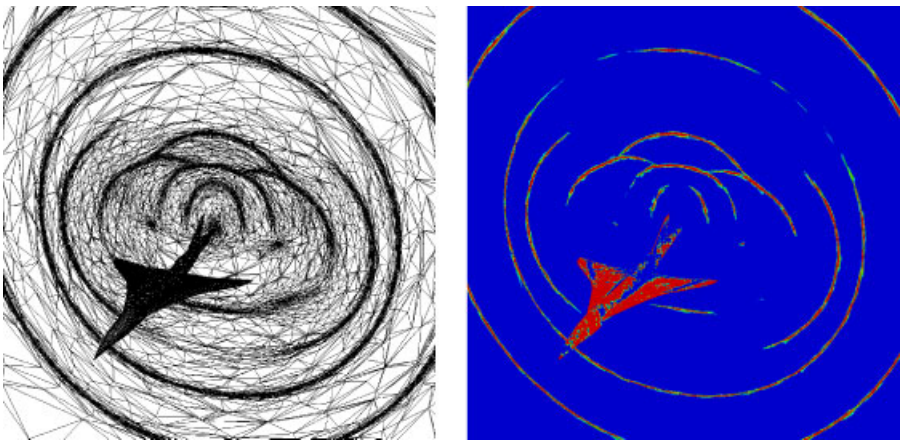

Figure 7. Perspective view of the mesh and elements K subject to the $h_{\min}$ criteria (TOL$=1.0$, $h_{\min}=0.1$).

This was confirmed by looking at cuts with planes in several other directions and for other values of TOL and $h_{\min}$ (not shown here). We recover the behavior predicted by the asymptotic analysis of Section 2.4. At shocks, $\lambda_{3,K}$ can never be small enough so that condition (11) is satisfied. Many elements K near the body of the aircraft are also subject to the $h_{\min}$ condition. Small elements may be required at the body because of the curvature of the geometry. Note that we do not have much control on the cell size along the aircraft surface because of the frozen skin mesh, but reducing $h_{\min}$ results in a smaller number of cells near the body subject to the $h_{\min}$ condition as we would expect.

Looking at the statistics of Table I and visualizing the mesh and solution from iteration to iteration as in Figures 4 and 5, one can see that we reach the 'algorithmic' convergence of the mesh and solution. We say 'algorithmic' convergence as mesh adaptation being a discrete process, one can never reach the exact same mesh from one iteration to the next. In the following sections, these criteria for algorithmic convergence will be used to decide whether enough mesher/solver iterations have been done.

3.3. Impact of the adaptation parameters TOL and $h_{\min}$

We first look at the effect of varying the parameter TOL appearing in the adaptation criteria (10) or (11). The minimal size $h_{\min}$ is kept constant and equal to 0.1. The parameter TOL is taken equal to 2.0, 1.0 and 0.5. The adaptation cycles for these three cases are started from the same initial mesh presented in Section 3.1. The results presented are for 50 mesher/solver iterations except when TOL$=1.0$ where we preferred to do 100 cycles to reach the algorithmic convergence of the mesh.

Figures 8 and 9 present the final adapted meshes and solutions for three values of TOL on the cut plane $y=0$ and $x=0$, respectively. Clearly, the solution is improved while decreasing TOL. For TOL$=2.0$, the conical shock created at the tip of the aircraft is meshed and seen close to the tip but rapidly fades out far from the aircraft. Several weaker shocks are missed such as the one generated by the wing/body junction, the one at the aircraft trailing edge and many shocks below the aircraft. In spite of the small number of nodes and cells for TOL$=2.0$ (see Table II),

DOI: 10.1002/fld

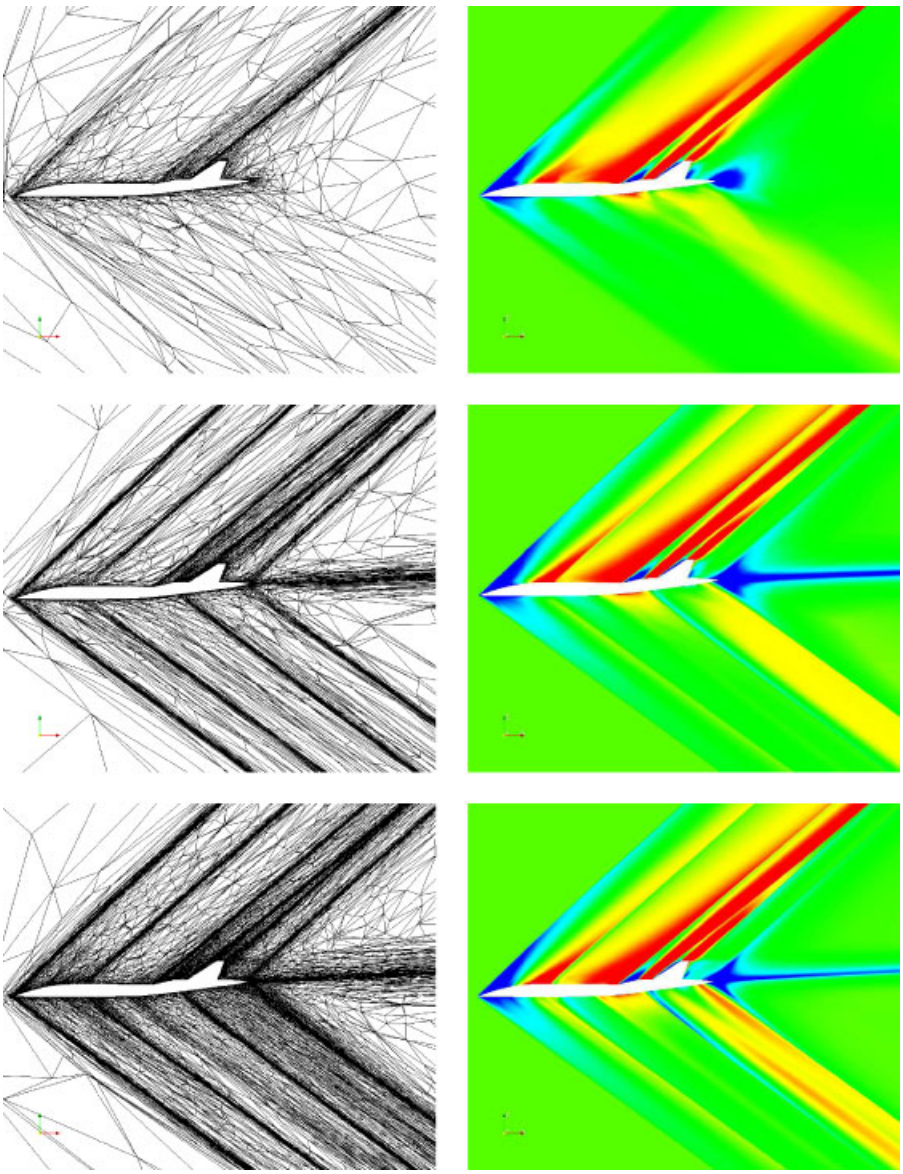

Figure 8. Mesh and local Mach number on the cut plane $y=0$: TOL$=2.0$ (top), TOL$=1.0$ (middle) and TOL$=0.5$ (bottom).

it is a surprise to see how well the flow features are resolved in the vicinity of the empennage and its upstream bump. These observations are confirmed by the graph of Figure 10 where the local Mach number is plotted as a function of the x-coordinates along a cut line (compare the blue curve with the red one). This cut line is on the symmetry plane of the aircraft and can be seen as a red segment on the upper figure.

DOI: 10.1002/fld

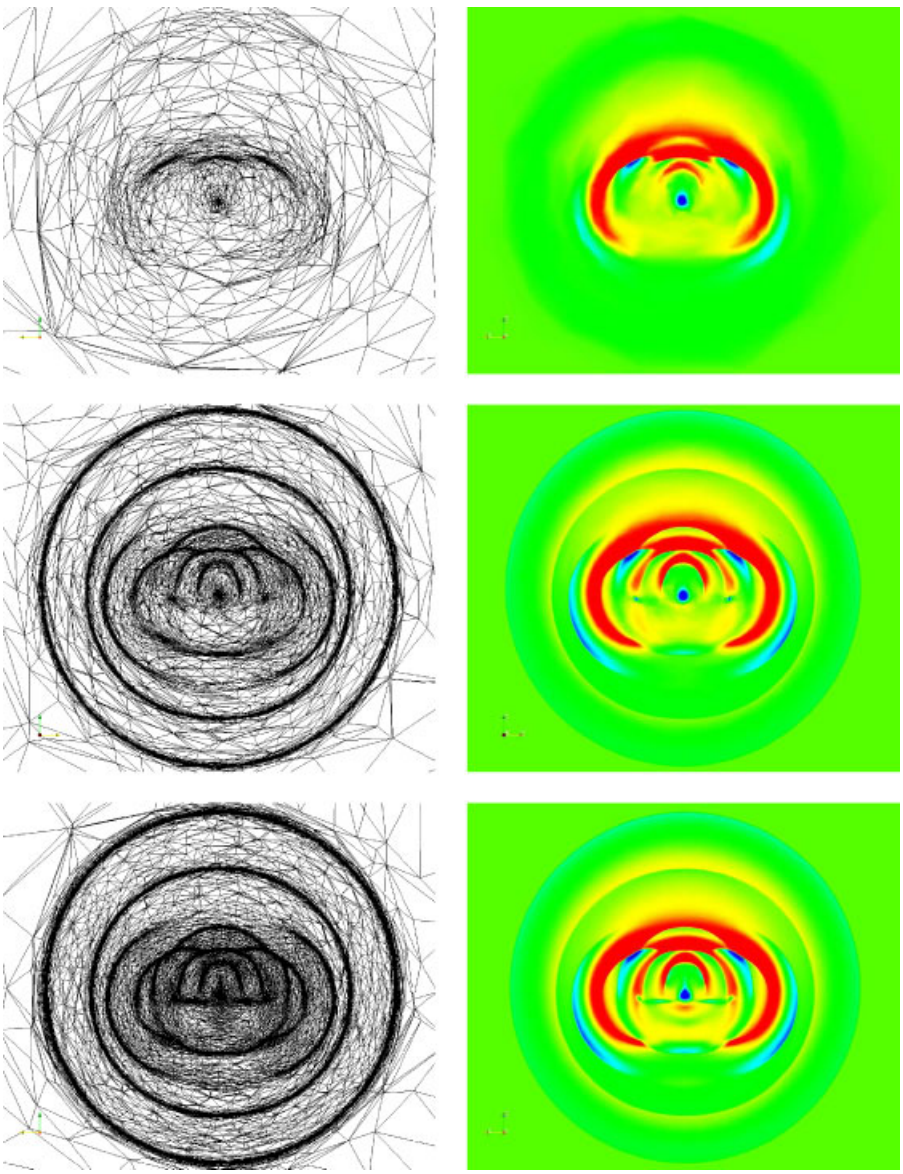

Figure 9. Mesh and local Mach number on the cut plane $x = 0$: TOL = 2.0 (top), TOL = 1.0 (middle) and TOL = 0.5 (bottom).

Decreasing TOL from 2.0 to 1.0, the number of nodes is multiplied almost by 4 and the number of tetrahedra by 5. We have not yet reached the asymptotic behavior where dividing TOL by 2 results in 8 times as many nodes or cells. The solution has greatly improved though. All the shock and rarefaction waves are now caught and meshed. This can be seen in Figures 8 and 9 but also by comparing the green and red curves on the graph of Figure 10. Compared with the curve for

DOI: 10.1002/fld

Table II. Mesh statistics for $h_{\min}=0.1$ and various TOL after 50 mesher/solver iterations.

TOL	0.5	1.0	2.0
No. nodes	1 193 575	194 533	50 549
No. tetrahedra	6 928 342	1 041 496	193 828
Average $\lambda_{1,K}$	1.79	4.09	4.34
Average $\lambda_{3,K}$	0.104	0.211	0.634
Average $\frac{\lambda_{1,K}}{\lambda_{3,K}}$	22.7	40.1	17.9
$\max_K \frac{\lambda_{1,K}}{\lambda_{3,K}}$	661.2	1507.1	346.8
$\min_K \mathrm{vol}(K)$	7.71e−8	4.99e−8	7.83e−8
$\max_K \mathrm{vol}(K)$	4.78e4	5.45e4	7.11e4
$\|\nabla M_h\|_{L^2(\Omega)}$	18.53	18.59	11.65
$(\sum_{K\in\mathcal{T}_h}\eta_K^2)^{1/2}/\|\nabla M_h\|_{L^2(\Omega)}$	0.784	0.990	1.196

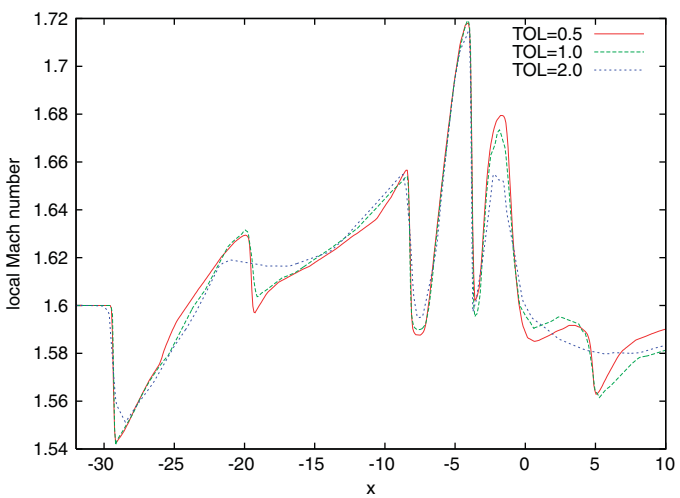

Figure 10. Plot of the local Mach number as a function of the x-coordinate on the line $(x, y, z)=(t, 0, 5)$ for $t\in[-32, 10]$—effect of varying TOL.

DOI: 10.1002/fld

our most accurate solution (the red curve for TOL$=0.5$ on this graph), the main differences are in the local maxima and minima that are not as high or low, respectively, for TOL$=1.0$. If we keep decreasing TOL from 1.0 to 0.5, the number of nodes is multiplied by 6 and the number of tetrahedra by 7. We are getting closer to the asymptotic behavior of these numbers with respect to TOL, if ever it can be achieved because of the application of the $h_{\min}$ condition. The general aspect of the solution is the same as for TOL$=1.0$. Small differences can be seen in the wake and below the aircraft in the back. It is not clear what is the exact mechanism behind these minor differences, especially for the wake that is in principle not well or at best only partially described by the Euler equations. Aside from these small differences, we are relatively convinced that if we keep decreasing TOL the solution would look the same to the eyes, both for iso-color plots and graphs generated from cut lines. Note that doing simulations for TOL<0.5 (with $h_{\min}=0.1$) would require more than the 2 GB of RAM available on a 32-bit system.

In Table II we compare various mesh statistics for three values of the parameter TOL. While discussing the number of nodes or cells with respect to TOL, we noted that the asymptotic behavior starts to be apparent for TOL$\leqslant 1.0$ in our simulations. This is confirmed by the average $\lambda_{1,K}$ and $\lambda_{3,K}$ that are approximately halved while going from TOL$=1.0$ to 0.5, figures that are consistent with a number of cells almost multiplied by 7. The tetrahedra near shock waves have a thickness of $h_{\min}$ across the shocks; hence the number of these tetrahedra is controlled by $h_{\min}$ as well. As $h_{\min}$ did not vary going from TOL$=1.0$ to 0.5, we should only expect to increase the number of cells or nodes by a factor smaller than 8. Note that if we keep decreasing TOL, we should consider decreasing $h_{\min}$ as well. Indeed the average $\lambda_{3,K}$ equals 0.104 for TOL$=0.5$, and $h_{\min}=0.1$ is about to limit $\lambda_{3,K}$ from below. The average tetrahedra aspect ratio, i.e. the average ratio $\lambda_{1,K}/\lambda_{3,K}$ increases while decreasing TOL down to a value where this ratio starts decreasing. As the average $\lambda_{3,K}$ approaches the lower bound $h_{\min}=0.1$, more and more tetrahedra are such that $\lambda_{3,K}=0.1$ whereas at the same time $\lambda_{1,K}$ and $\lambda_{2,K}$ are both getting smaller compared to results obtained with larger TOL. The anisotropy ratio is then limited by the value of $h_{\min}$. This calls again for a reduction of $h_{\min}$. All the other statistics presented seem to be independent to some extent from TOL. We guess from its values for TOL$\leqslant 1.0$ that $\|\nabla M_h\|_{L^2(\Omega)}$ is equal to 18.5 with three significant figures. Looking at Figure 6, we see that the ratio $(\sum_{K\in\mathcal{T}_h}\eta_K^2)^{1/2}/\|\nabla M_h\|_{L^2(\Omega)}$ that appears in the global adaptation criteria (10) converges to an asymptotic value. The asymptotic values for TOL$=0.5$, 1.0 and 2.0 are given in Table II. As expected from the asymptotic analysis of Section 2.4, the asymptotic value obtained through mesh adaptation is not necessarily in the interval $[0.75\,\text{TOL}, 1.25\,\text{TOL}]$ but it converges to a value controlled by both TOL and $h_{\min}$.

We next look at the effect of varying the minimal size $h_{\min}$ while keeping the adaptation parameter TOL constant. Our test cases will be done for TOL$=1.0$ and $h_{\min}=0.01$, 0.1 and 1.0. We proceed for these three test cases as for the test cases for studying the effect of TOL except that the adaptation cycle for $h_{\min}=0.01$ was initiated from the final adapted mesh and solution for $h_{\min}=0.1$.

Figures 11 and 12 present the final adapted meshes and solutions for three values of $h_{\min}$ on the cut plane $y=0$ and $x=0$, respectively. Obviously, taking $h_{\min}$ too large for a given TOL negatively affects the accuracy of the solution. Shock waves simply cannot be refined. Even if the number of nodes and cells are about the same as for TOL$=2.0$ and $h_{\min}=0.1$ (see Tables II and III), the solution is much worse with a large $h_{\min}$ and medium TOL than with a medium $h_{\min}$ and large TOL. Now decreasing $h_{\min}$, we see that the solution improves but only up to a point where TOL is the main parameter controlling the accuracy. For example, the meshes and solutions do

DOI: 10.1002/fld

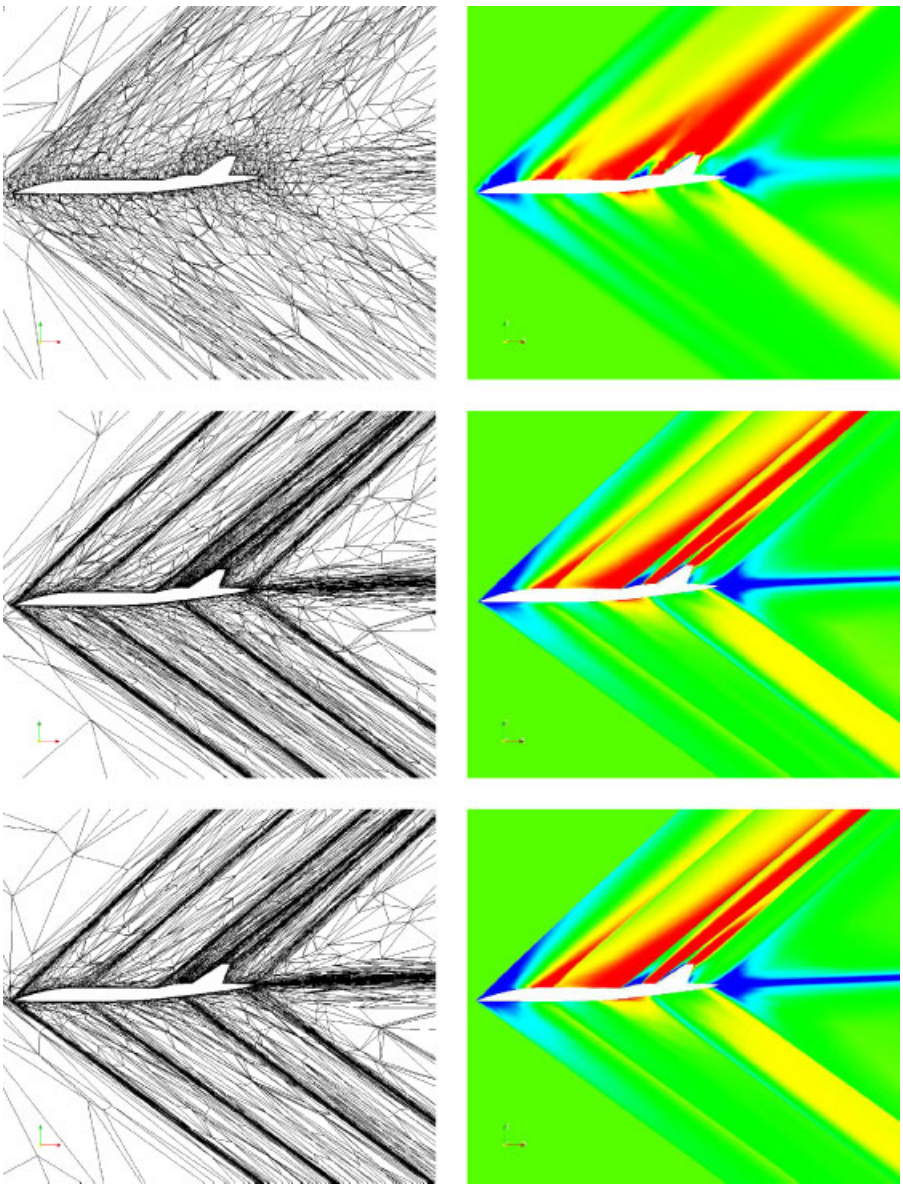

Figure 11. Mesh and local Mach number on the cut plane $y=0$: $h_{\min}=1.0$ (top), $h_{\min}=0.1$ (middle) and $h_{\min}=0.01$ (bottom).

not change much while decreasing $h_{\min}$ from 0.1 to 0.01, as seen in Figures 11 and 12. Regions with a smooth solution are meshed in a statistically identical way, in terms of both cell density and stretching, simply because the mesh adaptation is exclusively controlled by the local adaptation criteria (11) there. Only a blow-up of the mesh close to shock waves shows that the tetrahedra are about 10 times thinner along the normal to the shock for $h_{\min}=0.01$ compared with $h_{\min}=0.1$.

DOI: 10.1002/fld

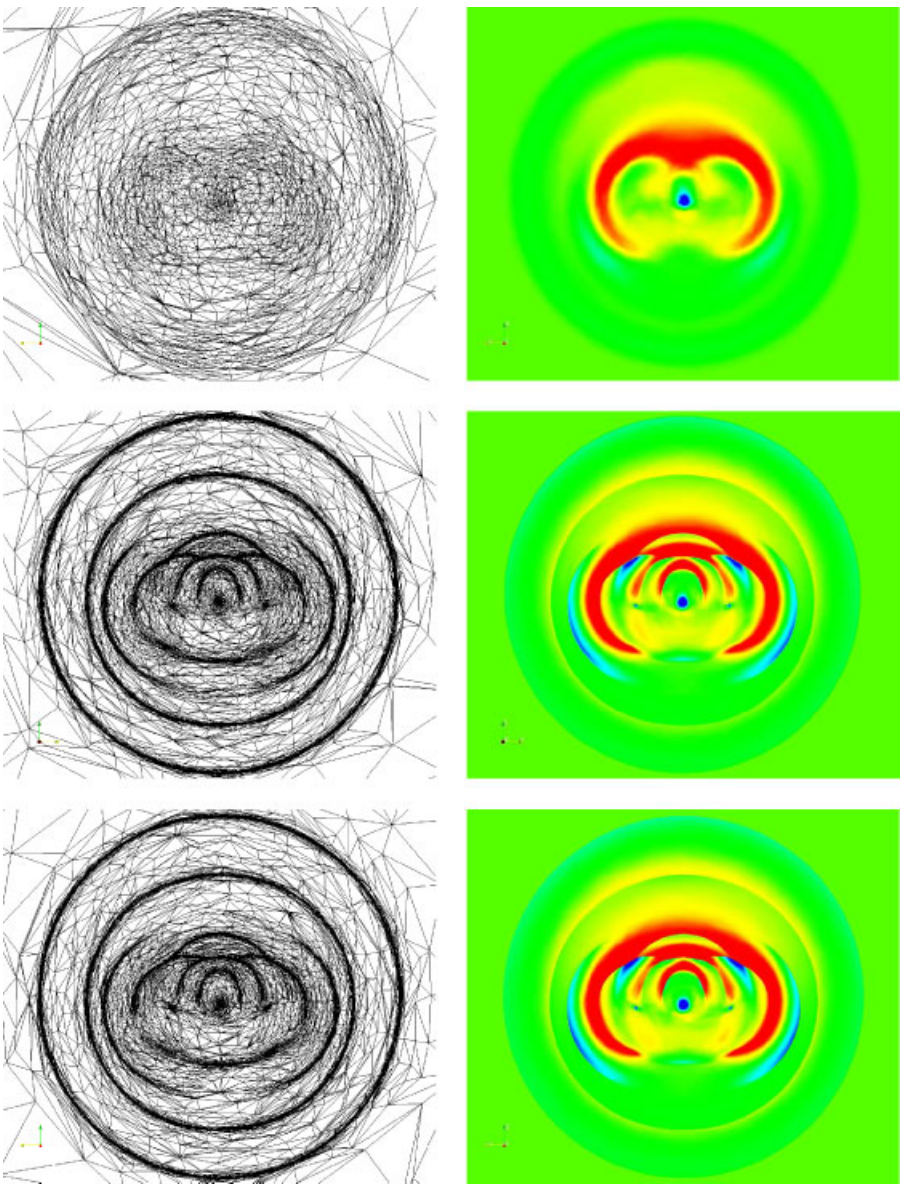

Figure 12. Mesh and local Mach number on the cut plane $x=0$: $h_{\min}=1.0$ (top), $h_{\min}=0.1$ (middle) and $h_{\min}=0.01$ (bottom).

These thinner cells improve the solution in shocks, with steeper slopes of the numerical solution (compare the blue and green graphs in Figure 13). The improvement is otherwise limited. Both graphs follow each other relatively closely but are consistently off the graph for TOL$=0.5$ in some regions where the solution is smooth. The solution for TOL$=0.5$ is certainly better in these regions because the adaptation criteria (11) works full fledgedly there.

DOI: 10.1002/fld

Table III. Mesh statistics for TOL = 1.0 and various $h_{\min}$ after 50 mesher/solver iterations.

$h_{\min}$	0.01	0.1	1.0
No. nodes	1 791 112	194 533	48 668
No. tetrahedra	10 451 960	1 041 496	182 360
Average $\lambda_{1,K}$	1.76	4.09	6.19
Average $\lambda_{3,K}$	0.0236	0.211	0.956
Average $\frac{\lambda_{1,K}}{\lambda_{3,K}}$	216.1	40.1	8.1
$\max_K \frac{\lambda_{1,K}}{\lambda_{3,K}}$	17659.1	1507.1	408.2
$\min_K \mathrm{vol}(K)$	5.03e−8	4.99e−8	1.21e−7
$\max_K \mathrm{vol}(K)$	6.02e4	5.45e4	5.54e4
$\|\nabla M_h\|_{L^2(\Omega)}$	64.58	18.59	5.54
$(\sum_{K\in\mathcal{T}_h} \eta_K^2)^{1/2}/\|\nabla M_h\|_{L^2(\Omega)}$	1.137	0.990	1.966

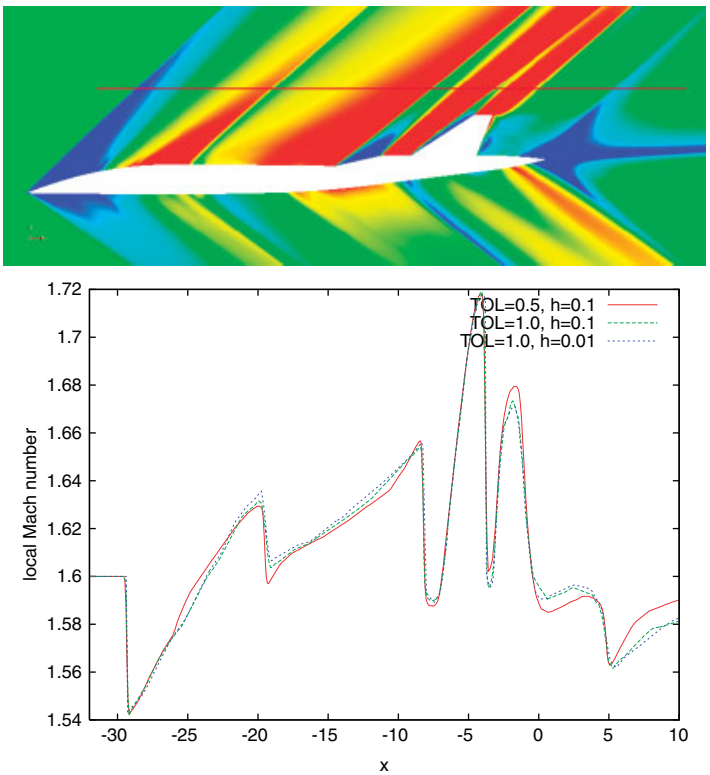

Figure 13. Plot of the local Mach number as a function of the x-coordinate on the line $(x, y, z) = (t, 0, 5)$ for $t \in [-32, 10]$—effect of varying $h_{\min}$ for TOL = 1.0. Comparison of these solutions with our most accurate solution obtained with TOL = 0.5 and $h_{\min} = 0.1$.

DOI: 10.1002/fld

In Table III we compare various mesh statistics for three values of the parameter $h_{\min}$. Most statistics depend strongly on $h_{\min}$. The norm $\|\nabla M_h\|_{L^2(\Omega)}$ behaves in $O(h^{-1/2})$, which implies that dividing $h_{\min}$ by 10 results in $\|\nabla M_h\|_{L^2(\Omega)}$ being multiplied by $\sqrt{10}\approx 3$. This is what we observed numerically. The ratio $(\sum_{K\in\mathscr{T}_h}\eta_K^2)^{1/2}/\|\nabla M_h\|_{L^2(\Omega)}$ is $O(1)$. Again this matches numerical experiments. Going from a $h_{\min}$ of 0.1 to 0.01, the number of nodes and cells are roughly multiplied by 10. As mentioned above, most new nodes are added around the solution discontinuities. Asymptotically, the number of nodes (respectively cells) around discontinuities dominates the total number of nodes (respectively cells) of the mesh, hence the behavior in $O(h^{-1})$ for these total numbers. The same reasoning applies to the average $\lambda_{3,K}$ that is asymptotically dominated by the tetrahedra of thickness $h_{\min}$ and that is roughly divided by 10 while going from a $h_{\min}$ of 0.1 to 0.01. On the other hand, $\lambda_{1,K}$ is controlled by criteria (11), hence by TOL, and does not vary significantly with $h_{\min}$. The combination of these two facts makes that the average or maximal stretching of the tetrahedra must grow with a decreasing $h_{\min}$. Again this is what we observed experimentally. The maximal and minimal volumes of the cells are not much affected by the value of $h_{\min}$.

3.4. Comparison with a priori error estimators

We compare meshes and solutions obtained with our *a posteriori* $H^1(\Omega)$-error estimator with the ones obtained with the *a priori* $L^p(\Omega)$-error estimators introduced in [13]. The idea is to calculate a metric tensor $\mathscr{M}=\mathscr{M}(P)$ as in Equation (12) with eigenvalues γ_i properly scaled so as to represent a mesh $\mathscr{T}_h$ minimizing the interpolation error $\|u-R_h u\|_{L^p(\Omega)}$ for a given number of nodes. Here R_h denotes the usual $P1$ Lagrange interpolation operator over the mesh $\mathscr{T}_h$. This Lagrange interpolant is well defined in functions u that are least in $C^0(\bar{\Omega})$, in particular functions that are in $H^2(\Omega)$ in dimension 3. As for our *a posteriori* estimator, this requires some extension of the *a priori* error estimators to act on piecewise regular functions and handle shock waves in inviscid flows.

We show only results for $p=1$, which corresponds to the most sensitive norm. A solution to improve accuracy in regions where the solution is not smooth consists in using L^p norms with larger values of p. Figure 14 shows the meshes and solutions on the cut plane $x=0$ for two test cases, one with 182 013 vertices and 976 292 tetrahedra that compares with the results for TOL = 1.0 in Figure 9 and the other with 1 096 446 vertices and 6 462 350 tetrahedra that compares with the results for TOL = 0.5 in the same figure. The number of nodes and cells in the respective test cases for the *a posteriori* estimator are given in Table II. The results for the *a priori* estimators have been computed targeting the same number of nodes as for the *a posteriori* estimator. The exact number of nodes are never achievable in practice because of the discrete nature of mesh adaptation algorithms. We imposed a $h_{\min}$ of 0.1 for the test case at the top of Figure 14 while no $h_{\min}$ was imposed for the test case at the bottom. A condition on $h_{\min}$ is not required with this L^1-error estimator, because of the appropriate scaling of the eigenvalues in the metric tensor $\mathscr{M}$. Comparing the figures, one concludes that both approaches are capable of producing the main features of this supersonic flow.

4. CONCLUSIONS

We have applied an *a posteriori* error estimator for controlling a metric-based anisotropic mesh adaptation software to improve numerical solutions for 3D inviscid flows around a supersonic

DOI: 10.1002/fld

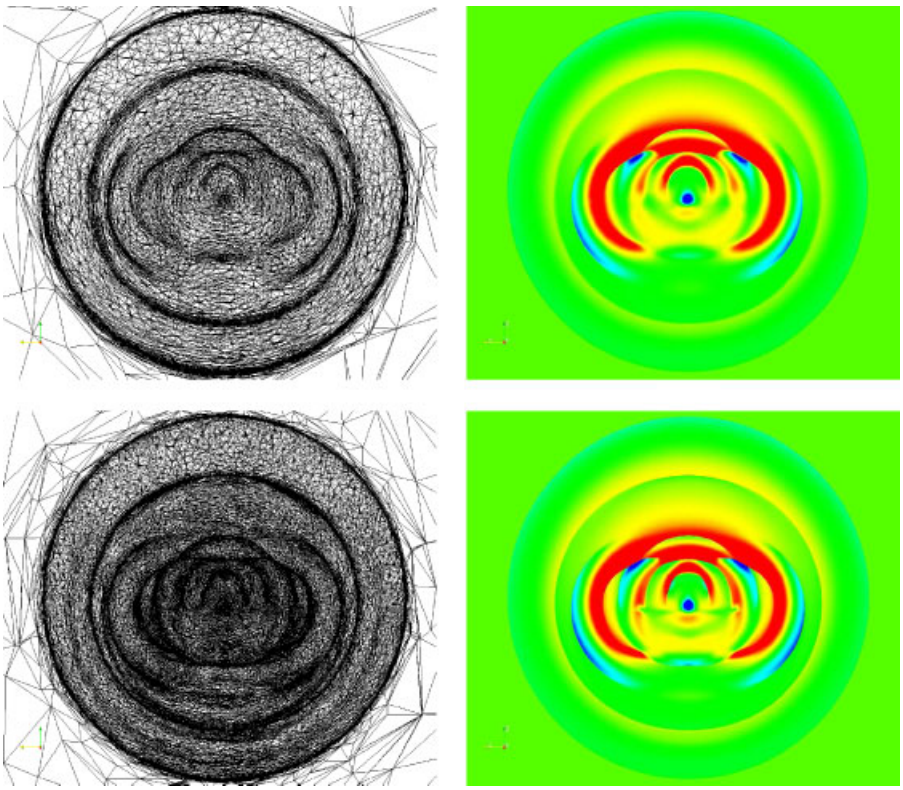

Figure 14. Mesh and local Mach number on the cut plane $x=0$ obtained using an *a priori* L^1-error estimator: 182 013 vertices and 976 292 tetrahedra (top), 1 096 446 vertices and 6 462 350 tetrahedra (bottom).

aircraft. The results turn out to be spectacular in spite of the fact that the use of these error estimators cannot be fully justified for solutions with shock and contact discontinuities. For instance, the *a posteriori* error estimator used is funded from a theoretical standpoint for elliptic problems with solutions in $H^{1+\varepsilon}(\Omega)$ for some $\varepsilon>0$. For solutions to the Euler equations with shocks we are certainly far from this hypothesis.

We have identified a strategy based on the imposition of a minimal edge length $h_{\min}$ over the mesh to extend the applicability of our *a posteriori* error estimator to solutions with discontinuities, at least from a practical standpoint. In regions of the domain Ω where the solution is regular, the mesh adaptation is controlled by a local adaptation criteria based on the parameter TOL. The local adaptation criteria equidistribute the H^1-error over the tetrahedra in these regions of the domain. Around solution discontinuities, we showed through an asymptotic analysis in $h_{\min}$ that the local adaptation criteria should fail in the direction normal to the shock. As a remedy we proposed to replace the local adaptation criteria by the imposition of a minimal grid size $h_{\min}$ but only in the direction normal to the discontinuity. We verified that the asymptotic behavior is observed in numerical experiments by conducting test cases with three different values of $h_{\min}$ for the same value of TOL. This gave some hints on the selection of consistent values of TOL and $h_{\min}$ to

DOI: 10.1002/fld

guarantee the efficiency of the anisotropic mesh adaptation. Basically, $h_{\min}$ must be small enough for a given TOL so that the $h_{\min}$ condition applies only at discontinuities but not too small so that most tetrahedra are thrown at the discontinuities, increasing amazingly the computational cost for a marginal gain in accuracy. Finally, we verified experimentally that reducing the parameter TOL can improve the accuracy of the solutions up to the point where we can compute *mesh-independent 3D inviscid compressible flows over a full aircraft* using a desktop PC or a good laptop in a few days.

We compared the solutions obtained with our *a posteriori* error estimator to those obtained with *a priori* estimators. So far most of the attempts at anisotropic mesh adaptation for inviscid compressible flows were done with *a priori* estimators. Except for minor differences seen on meshes with fewer nodes, both approaches gave consistently good results. It is comforting to see that an *a posteriori* error estimator can be reliably used for such applications. More analysis is required though to do an in-depth comparison of the two approaches and better evaluate the merit of each error estimation strategy.

ACKNOWLEDGEMENTS

The authors would like to thank D. Alleau and J. P. Figeac from Dassault Aviation for their fruitful discussions and advices in the course of this work. P. Frey and C. Dobrzynski are acknowledged for providing the mesh adaptation tool `mmg3d` used for our simulations. This work was conducted when the corresponding author was visiting the Chair of Numerical Analysis and Simulation (Prof. J. Rappaz)—Institute of Analysis and Scientific Computing (IACS) at the Ecole Polytechnique Fédérale de Lausanne from August 2006 to July 2007.

REFERENCES

1. Almeida RC, Feijóo RA, Galeão AC, Padra C, Silva RS. Adaptive finite element computational fluid dynamics using an anisotropic error estimator. *Computer Methods in Applied Mechanics and Engineering* 2000; **182**(3–4):379–400 (*IV WCCM*, Buenos Aires, 1998).
2. Castro-Díaz MJ, Hecht F, Mohammadi B, Pironneau O. Anisotropic unstructured mesh adaption for flow simulations. *International Journal for Numerical Methods in Fluids* 1997; **25**(4):475–491.
3. Dompierre J, Vallet M-G, Bourgault Y, Fortin M, Habashi WG. Anisotropic mesh adaptation: towards user-independent, mesh-independent and solver-independent CFD. III. Unstructured meshes. *International Journal for Numerical Methods in Fluids* 2002; **39**(8):675–702.
4. Habashi WG, Fortin M, Dompierre J, Vallet M-G, Bourgault Y. Certifiable CFD through mesh optimization. *American Institute of Aeronautics and Astronautics Journal* 1998; **36**(5):703–711.
5. Fortin M, Habashi WG, Vallet M-G, Dompierre J, Bourgault Y, Ait-Ali-Yahia D. Anisotropic mesh adaptation: towards user-independent, mesh-independent and solver-independent CFD. Part I: general principles. *International Journal for Numerical Methods in Fluids* 2000; **32**:725–744.
6. Frey PJ, George P-L. *Mesh Generation. Application to Finite Elements*. Hermès Science: Paris, Oxford, 2000.
7. D'Azevedo EF. Optimal triangular mesh generation by coordinate transformation. *SIAM Journal on Scientific and Statistical Computing* 1991; **12**(4):755–786.
8. D'Azevedo EF, Simpson RB. On optimal interpolation triangle incidences. *SIAM Journal on Scientific and Statistical Computing* 1989; **10**(6):1063–1075.
9. Alauzet F, Frey PJ, George P-L, Mohammadi B. 3D transient fixed point mesh adaptation for time-dependent problems: application to CFD simulations. *Journal of Computational Physics* 2007; **222**:592–623.
10. Frey PJ, Alauzet F. Anisotropic mesh adaptation for CFD computations. *Computer Methods in Applied Mechanics and Engineering* 2005; **194**(48–49):5068–5082.
11. Remaki L, Habashi WG. 3-D mesh adaptation on multiple weak discontinuities and boundary layers. *SIAM Journal on Scientific and Statistical Computing* 2006; **28**(4):1379–1397.
12. Belhamadia Y, Fortin A, Chamberland É. Three-dimensional anisotropic mesh adaptation for phase change problems. *Journal of Computational Physics* 2004; **201**(2):753–770.

DOI: 10.1002/fld

13. Loseille A, Dervieux A, Frey PJ, Alauzet F. Achievement of global second-order mesh convergence for discontinuous flows with adapted unstructured meshes. *AIAA Paper 2007-4186*, 2007.
14. Formaggia L, Perotto S. New anisotropic a priori error estimates. *Numerische Mathematik* 2001; **89**(4):641–667.
15. Formaggia L, Perotto S. Anisotropic error estimates for elliptic problems. *Numerische Mathematik* 2003; **94**:67–92.
16. Kunert G. An a posteriori residual error estimator for the finite element method on anisotropic tetrahedral meshes. *Numerische Mathematik* 2000; **86**(3):471–490.
17. Kunert G. A posteriori L_2 error estimation on anisotropic tetrahedral finite element meshes. *IMA Journal of Numerical Analysis* 2001; **21**(2):503–523.
18. Picasso M. Numerical study of the effectivity index for an anisotropic error indicator based on Zienkiewicz–Zhu error estimator. *Communications in Numerical Methods in Engineering* 2002; **19**:13–23.
19. Picasso M. An anisotropic error indicator based on Zienkiewicz–Zhu error estimator: application to elliptic and parabolic problems. *SIAM Journal on Scientific and Statistical Computing* 2003; **24**:1328–1355.
20. Picasso M. Adaptive finite elements with large aspect ratio based on an anisotropic error estimator involving first order derivatives. *Computer Methods in Applied Mechanics and Engineering* 2006; **196**(1):14–23.
21. Burman E, Jacot A, Picasso M. Adaptive finite elements with high aspect ratio for the computation of coalescence using a phase-field model. *Journal of Computational Physics* 2004; **195**(1):153–174.
22. Burman E, Picasso M. Anisotropic, adaptive finite elements for the computation of a solutal dendrite. *Interfaces and Free Boundaries* 2003; **5**:103–127.
23. Formaggia L, Micheletti S, Perotto S. Anisotropic mesh adaption in computational fluid dynamics: application to the advection–diffusion–reaction and the Stokes problems. *Applied Numerical Mathematics* 2004; **51**(4):511–533.
24. Micheletti S, Perotto S, Picasso M. Stabilized finite elements on anisotropic meshes: a priori error estimates for the advection–diffusion and the Stokes problems. *SIAM Journal on Numerical Analysis* 2003; **41**(3):1131–1162.
25. Narski J, Picasso M. Adaptive 3d finite elements with high aspect ratio for dentritic growth of a binary alloy including flow induced by shrinkage. *Fluid Dynamics and Material Processing* 2007; **3**(1):49–64.
26. Houston P, Rannacher R, Süli E. A posteriori error analysis for stabilised finite element approximations of transport problems. *Computer Methods in Applied Mechanics and Engineering* 2000; **190**(11–12):1483–1508.
27. Houston P, Mackenzie JA, Süli E, Warnecke G. A posteriori error analysis for numerical approximations of Friedrichs systems. *Numerische Mathematik* 1999; **82**(3):433–470.
28. Süli E, Houston P. Adaptive finite element approximation of hyperbolic problems. *Error Estimation and Adaptive Discretization Methods in Computational Fluid Dynamics*. Lecture Notes in Computer Science and Engineering, vol. 25. Springer: Berlin, 2003; 269–344.
29. Cockburn B. A simple introduction to error estimation for nonlinear hyperbolic conservation laws. Some ideas, techniques, and promising results. *The Graduate Student's Guide to Numerical Analysis '98* (*Leicester*). Springer Series in Computational Mathematics, vol. 26. Springer: Berlin, 1999; 1–45.
30. Cockburn B. Continuous dependence and error estimation for viscosity methods. *Acta Numerica* 2003; **12**: 127–180.
31. Johnson C, Szepessy A. Adaptive finite element methods for conservation laws based on a posteriori error estimates. *Communications on Pure and Applied Mathematics* 1995; **48**(3):199–234.
32. Kröner D, Ohlberger M. A posteriori error estimates for upwind finite volume schemes for nonlinear conservation laws in multidimensions. *Mathematics of Computation* 2000; **69**(229):25–39.
33. Sonar T, Süli E. A dual graph-norm refinement indicator for finite volume approximations of the Euler equations. *Numerische Mathematik* 1998; **78**(4):619–658.
34. Alauzet F. Adaptive sonic boom sensitivity analysis. *European Conference on Computational Fluid Dynamics—ECCOMAS CFD 2006*, Egmond ann Zee, The Netherlands, September 2006.
35. Dobrzynski C. Adaptation de maillage anisotrope 3D et application à l'aéro-thermique des bâtiments. *Ph.D. Thesis*, Université Pierre et Marie Curie, Paris VI, Paris, France, 2005.
36. Cournède P-H, Koobus B, Dervieux A. Positivity statements for a mixed-element-volume scheme on fixed and moving grids. *European Journal of Computational Mechanics* 2006; **15**(7–8):767–798.
37. Stoufflet B, Periaux J, Fezoui L, Dervieux A. Numerical simulation of 3-D hypersonic Euler flows around space vehicles using adapted finite element. *AIAA Paper 87-0560*, 1987.
38. Batten P, Clarke N, Lambert C, Causon DM. On the choice of wavespeeds for the HLLC Riemann solver. *SIAM Journal on Scientific Computing* 1997; **18**(6):1553–1570.
39. Debiez C, Dervieux A. Mixed-element-volume MUSCL methods with weak viscosity for steady and unsteady flow calculations. *Computers and Fluids* 2000; **29**:89–118.
40. Spiteri RJ, Ruuth SJ. A new class of optimal high-order strong-stability-preserving time discretization methods. *SIAM Journal on Numerical Analysis* 2002; **40**(2):469–491.

DOI: 10.1002/fld

41. Kunert G, Verfürth R. Edge residuals dominate a posteriori error estimates for linear finite element methods on anisotropic triangular and tetrahedral meshes. *Numerische Mathematik* 2000; **86**(2):283–303.
42. Ainsworth M, Zhu JZ, Craig AW, Zienkiewicz OC. Analysis of the Zienkiewicz–Zhu a posteriori error estimator in the finite element method. *International Journal for Numerical Methods in Engineering* 1989; **28**(9):2161–2174.
43. Zienkiewicz OC, Zhu JZ. A simple error estimator and adaptive procedure for practical engineering analysis. *International Journal for Numerical Methods in Engineering* 1987; **24**(2):337–357.
44. Ainsworth M, Oden JT. A posteriori error estimation in finite element analysis. *Computer Methods in Applied Mechanics and Engineering* 1997; **142**(1–2):1–88.
45. Brandts J, Křížek M. Gradient superconvergence on uniform simplicial partitions of polytopes. *IMA Journal of Numerical Analysis* 2003; **23**(3):489–505.
46. Carstensen C. All first-order averaging techniques for a posteriori finite element error control on unstructured grids are efficient and reliable. *Mathematics of Computation* 2004; **73**(247):1153–1165.
47. Kunert G, Nicaise S. Zienkiewicz–Zhu error estimators on anisotropic tetrahedral and triangular finite element meshes. *Mathematical Modelling and Numerical Analysis* 2003; **37**(6):1013–1043.
48. Rodríguez R. Some remarks on Zienkiewicz–Zhu estimator. *Numerical Methods for Partial Differential Equations* 1994; **10**(5):625–635.
49. Wu H, Zhang Z. Can we have superconvergent gradient recovery under adaptive meshes? *SIAM Journal on Numerical Analysis* 2007; **45**(4):1701–1722.
50. Xu J, Zhang Z. Analysis of recovery type a posteriori error estimators for mildly structured grids. *Mathematics of Computation* 2003; **73**(247):1139–1152.
51. Dafermos CM. *Hyperbolic Conservation Laws in Continuum Physics* (2nd edn). Grundlehren der Mathematischen Wissenschaften (Fundamental Principles of Mathematical Sciences), vol. 325. Springer: Berlin, 2005.
52. Serre D. *Systems of Conservation Laws 1*: *Hyperbolicity*, *Entropies*, *Shock Waves*. Cambridge University Press: Cambridge, 1999 (Translated from the 1996 French original by I. N. Sneddon).

DOI: 10.1002/fld